UNIVERSITY OF CALIFORNIA
RIVERSIDE

Mechanical and Electrical Properties of Modified Graphene Devices

A Dissertation submitted in partial satisfaction
of the requirements for the degree of

Doctor of Philosophy

in

Physics

by

Hang Zhang

December 2012

Dissertation Committee:

Dr. Chun Ning (Jeanie) Lau, Chairperson
Dr. Robert C. Haddon
Dr. Jing Shi

The Dissertation of Hang Zhang is approved:

_____

_____

_____

Committee Chairperson

University of California, Riverside

Acknowledgment

First of all I would like to thank my advisor Prof. Chun Ning Lau. In the past five years, she taught me not only how to design experiments, how to use delicate equipment and how to analyze experimental data, but also how to consider a problem with physics pictures. It was really precious experience for me to learn and make discoveries under her supervision. Also, I want to thank my advisor in chemistry, Prof. Robert C. Haddon. His instruction on chemistry provided me a broaden vision on interdisciplinary researches and helped me finished some interesting projects. I have to say “Thank you!” to Prof. Marc Bockrath, too. I learned a lot from his creative thoughts on physical experiments. I also would like to thank Prof. Jing Shi. His class on nano-scale systems taught me latest knowledge and advanced investigating approaches in my research field.

I would like to thank my colleagues and friends, Elena Bekyarova, Santanu Sarkar, Xiaoliu Chi, Brian Standley, Feng Miao, Gang Liu, Wenzhong Bao, Jairo Velasco Jr., Zeng Zhao, Lei Jing, Jhao-Wun Huang, Fenglin Wang, Yongjin Lee, Kevin Myhro, Yanmeng Shi, Nathaniel Gilgren, Yong Pu, Feihu Wang, Dong Yan, Dexter Humphrey. Without your help and efforts, I cannot obtain these discoveries.

I am grateful to my parents. They always encouraged me to conquer barriers in my research.

ABSTRACT OF THE DISSERTATION

Mechanical and Electrical Properties on Modified Graphene Flakes

by

Hang Zhang

Doctor of Philosophy, Graduate Program in Physics
University of California, Riverside, December 2012
Dr. Chun Ning (Jeanie) Lau, Chairperson

Compared with traditional semiconductor materials, graphene has unparalleled advantages on mobility, thermal conductivity, mechanical strength and so on. Thus it was considered as a promising candidate material for the future semiconductor industry. However, since its band structure is gapless, band gap engineering has become a significant task for scientists. My dissertation focuses on chemical and physical modification methods that could pave the way to applications of graphene based devices and reveal a number of interesting phenomena.

The critical roadblock for graphene electronics is the absence of a band gap. We first focus on chemical functionalization of graphene as a route to band gap engineering. This is first achieved via grafting nitrophenyl groups onto single layer graphene sheets. The functionalized graphene samples behave like

semiconductors. Substrate supported and suspended samples demonstrate transport gaps as large as ~0.1eV and ~1eV, respectively. Secondly, we developed a different chemical functionalization approach based on organometallic chemistry. Apart from behaving like semiconductors, functionalized samples also retains the high mobility of the pristine state.

The second part of the thesis focuses on physical modifications of graphene a. Suspended graphene-based switch was developed using a special pulsing breakdown technique. Voltage pulses of 2.5V~4V and 8V can turn a switch device to ON (high conductance) state and OFF (low conductance) state, respectively. We provide experimental evidence that these behaviors arise from motions of atomic-scale carbon chains and reformation of chemical bonds.

Finally, strain engineering is another approach for modifying transport properties of graphene. We proposed and developed novel nano-electromechanical system (NEMS)-like devices that allows *in situ* modulation of strain on suspended graphene flakes, which in turn induces interesting changes in both transport and morphological properties of graphene. In summary, this dissertation presents our studies on chemical and physical modification approaches of graphene samples, and related novel phenomena that emerge amid these devices, with implications on next generation electronic devices.

Table of Contents

Chapter 1. Introduction ..…….. 1

Chapter 2. Background …… 6

2.1 The History of Graphene ..…….…… 6

2.2 The Unique Dispersion Relation of Graphene ...……..… 7

2.3 Synthesis of large scale graphene and the applications ...…….16

Chapter 3. Sample Preparation and Device Fabrication……..… 20

3.1 Sample (graphene) preparation, localization and identification ..…… 20

3.2 Device Fabrication ……...22

Chapter 4. Aryl functionalization in single layer graphene devices ……..… 28

4.1 Band Gap Engineering and Functionalized Graphene …… 29

4.2 Device Fabrication and Functionalization Process ……..…...… 31

4.3 Mechanisms of Transport properties …….……..… 36

4.4 Suspended Samples ……...…….…… 41

Chapter 5. Organometallic Hexahapto Functionalization of Single Layer Graphene Devices ……51

5.1 Organometallic Hexahapto Functionalization …...……..… 51

5.2 Experiment Setup and Procedures ……...…… 57

5.3 Transport Features ……...…… 60

5.4. Conclusion ……...……..…… 68

Chapter 6. Suspended graphene based switch……..74

6.1 Electronic Breakdown in Carbon System……..……...75

6.2 Device Fabrication and Breakdown Process ……..……..77

6.3 Measurement and Mechanisms……..…….....80

Chapter 7. Transport in Suspended graphene under strain…….....92

7.1 Device Design and Fabrication……..…….....93

7.2 Transport Properties Under *in situ* Train…….....…. 99

7.3 Possible Mechanisms…….……..…….....103

Chapter 8. Conclusion and Outlook……...……107

Appendix I. Source Code and introduction of Graphene Layer Viewer…..110

List of Figures

Figure 2.1. Geometry operation can convert graphene into 0D buckyball, 1D carbon nano-tube and 3D graphite ……..…… . 7

Figure 2.2 Crystal structure and Bravais lattice of graphene ……9

Figure 2.3 The honeycomb crystal structure of monolayer graphene ……...… 12

Figure 2.4 The 3-D view of band structure of single layer graphene …… 14

Figure 2.5 The Brillouin zone of hexagonal lattice …….……...… 14

Figure 3.1 Optical image of Single and double layer graphene samples on top of a Si/SiO_2 wafer…….……..……... . 21

Figure 3.2 Device fabrication….……..…….….25

Figure 4.1 *I-V* and $G(V_g)$ characteristics of a pristine graphene, functionalization process and Raman characterization ……...……...……....32

Figure 4.2 Transport data of NS1 after functionalization ……..…….....34

Figure 4.3 T-dependent transport data of NS1…..……..40

Figure 4.4 SEM image and transport data of a suspended graphene device …..44

Figure 5.1 Organometallic functionalization of single-layer graphene devices……...55

Figure 5.2 Organometallic functionalization of graphene and graphite …….57

Figure 5.3 Transport data of a single layer graphene device before and after

functionalization ……..…..……...…..61

Figure 5.4 Transport data of a lightly functionalized graphene device…....…..64

Figure 5.5 Decomplexation of chromium-graphene complexes …....……...65

Figure 5.6 *I-V* curves at Dirac point of a pristine graphene device at T = 300 K and 4.5 K ……..……..…..……..67

Figure 5.7 Zero bias conductance *vs.* temperature at both Dirac Point and Highly doped region……...……..…..……...…..68

Figure 6.1 *IV−time* curves of a suspended graphene device during breakdown…. .78

Figure 6.2 *In situ* SEM images of a suspended graphene device during breakdown……..80

Figure 6.3 Current and conductance response during switch cycles and *in situ* SEM images at ON and OFF state..……..…….82

Figure 6.4 Typical current response versus time in a single switching cycle at different temperatures ……86

Figure 6.5 Average waiting time *vs.* temperature and statistical analysis of the waiting time ……...……87

Figure 7.1 Fabrication process of two type of devices. ……..94

Figure 7.2 Schematics and *in situ* SEM images of devices before stretching, under strain and after stretching process.....98

Figure 7.3 Transport data of single layer graphene devices before stretching, under strain and after stretching process ……..…..…..100

Figure 7.4 Transport data of bi-layer graphene devices before and after stretching process and an SEM image after stretching process……102

Chapter 1

Introduction

Graphene is the single atomic layer of planar sheet of sp^2-bonded carbon atoms that are arranged in a honeycomb crystal lattice. Since its first experimental isolation on insulating substrates[1] and the development of a wafer scale growth technology,[2] graphene has rapidly become a promising candidate for next generation electronic material.[3] Its material properties, such as atomically thin dimension, unparalleled room-temperature mobility,[4-8] thermal conductivity,[9] and current carrying capacity,[10] are far superior to those of silicon, whereas its two-dimensionality (2D) is naturally compatible with standard CMOS-based technologies. However, since graphene is a gapless semiconductor, it cannot be readily applied in digital electronic devices. Therefore, more research tasks are necessary to open a band gap in this “wonder material”, so that it may replace Si for continuing miniaturization of next generation electronic devices.

In this dissertation, we will demonstrate several experiments on gap engineering of graphene (opening a real band gap or transport gap in pristine

graphene samples), which have direct implications for graphene electronics. Additionally, we have also discovered some new properties of graphene sheets via *in situ* measurement and developed new tools which will contribute to future investigation on nanoscale materials.

The thesis is organized as following. Chapter 2 presents the background of graphene electronics, including graphene's lattice structure, band structure by tight bonding model, and physics properties. Chapter 3 describes detailed steps of selecting graphene samples and device fabrication, which constitute an important part of our studies. Chapter 4 demonstrates aryl functionalization, a simple but very useful chemical functionalization method, on single layer graphene devices. This chemical treatment can controllably graft aryl groups onto carbon atoms in graphene sheet, changing the original sp^2 hybridization into sp^3, which, in turn, modifies the band structure of graphene or even open a real band gap. As a result, the functionalized sample will behave like semiconductor. In Chapter 5, I will present another important functionalization method: Cr functionalization on single layer graphene devices. Apart from the enhanced on/off ratio, we can also retain high mobility from pristine graphene devices. In Chapter 6, I will discuss a switch device made from suspended graphene. With the help of electro-migration method, we create suspended graphene based switches. In addition to studies on device performances, we reveal mechanism of behaviors of our switches by *in situ*

imaging and transport measurement. This project also provides potential application in long term information storage from all-carbon-devices. Chapter 7 discusses suspended graphene samples under *in situ* strain. We develop a new type of nano-electromechanical system (NEMS) which allows transport studies in the presence of applied strain. We obtain interesting results from transport measurement and *in situ* SEM imaging. In the last chapter, Chapter 8, I will summarize and discuss future follow-up experiments and outlooks for the field of graphene electronics.

References:

1 Novoselov, K. S.; Geim, A. K.; Morozov, S. V.; Jiang, D.; Zhang, Y.; Dubonos, S. V.; Grigorieva, I. V.; Firsov, A. A. *Science* **2004,** *306* (5296), 666–669.

2 Berger, C.; Song, Z. M.; Li, X. B.; Wu, X. S.; Brown, N.; Naud, C.; Mayo, D.; Li, T. B.; Hass, J.; Marchenkov, A. N.; Conrad, E. H.; First, P. N.; de Heer, W. A. *Science* **2006,** *312* (5777), 1191–1196.

3 Fuhrer, M. S.; Lau, C. N.; MacDonald, A. H. *MRS Bull.* **2010,** *35*(4), 289–295.

4 Novoselov, K. S.; Geim, A. K.; Morozov, S. V.; Jiang, D.; Katsnelson, M. I.; Grigorieva, I. V.; Dubonos, S. V.; Firsov, A. A. *Nature* **2005,** *438* (7065), 197–200.

5 Zhang, Y. B.; Tan, Y. W.; Stormer, H. L.; Kim, P. *Nature* **2005,** *438* (7065), 201–204.

6 Chen, J. H.; Jang, C.; Xiao, S. D.; Ishigami, M.; Fuhrer, M. S. *Nat. Nanotechnol.* **2008,** *3* (4), 206–209.

7 Bolotin, K. I.; Sikes, K. J.; Jiang, Z.; Klima, M.; Fudenberg, G.; Hone, J.; Kim, P.; Stormer, H. L. *Solid State Commun.* **2008,** *146* (9_10), 351–355.

8 Du, X.; Skachko, I.; Barker, A.; Andrei, E. Y. *Nat. Nanotechnol.* **2008,** *3* (8), 491–495.

9 Balandin, A. A.; Ghosh, S.; Bao, W.; Calizo, I.; Teweldebrhan, D.; Miao, F.; Lau, C. N. *Nano Lett.* **2008,** *8,* 902.

10 Standley, B.; Bao, W.; Zhang, H.; Bruck, J.; Lau, C. N.; Bockrath, M. *Nano Lett.* **2008,** *8,* 3345.

Chapter 2

Background

2.1 The History of Graphene

Carbon plays an important role in the world of condensed matter physics. In 0-dimension (0D), it forms buckyballs; in 1-dimension (1D), it is the famous carbon nanotube (CNT); when it was piled up to 3-dimension (3D), it becomes ubiquitous and is known as graphite. In 2004, the 2-dimensional (2D) member of this family, graphene, was exfoliated from graphite onto an insulating substrate by Professor A. K. Geim's research group in UK[1]. Graphene became an extremely popular material virtually overnight and generated an explosion of interest from scientists in condensed matter physics.

Graphene is a single atomic layer of carbon atoms in a hexagonal lattice. The relationship between graphene and 0D, 1D and 3D carbon systems is shown in Figure 2.1. Before the discovery of this material, graphene was considered as nonexistent in the real world, since scientists thought that finite temperature induces atom dislocation or lattice defects that will destroy the 2D crystals.[2,3]

However, the isolation of single layer graphene sheets demonstrates that the covalent bonds between carbon atoms are strong enough to withstand thermal fluctuations and maintain the hexagon lattice.

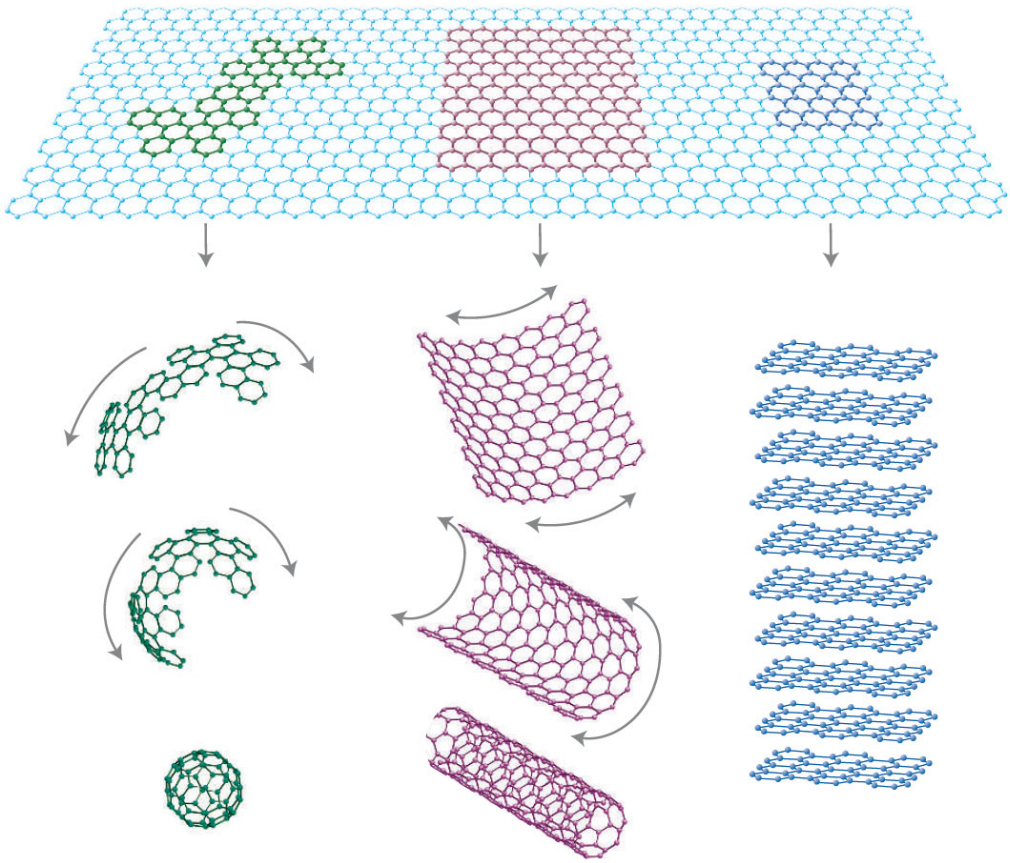

FIGURE 2.1. Geometry operation can convert graphene into 0D buckyball, 1D carbon nano-tube and 3D graphite.[4]

2.2 The Unique Dispersion Relation of Graphene

In 1947, Wallace first predicted the band structure of graphene.[5] The dispersion relation can be calculated by tight binding model approach [6]. A detailed

derivation is given in McCann's recent review paper (ref. 6).

Single layer graphene has a 2-dimensional honeycomb crystal structure (See Figure 2.2 (a)). The basis of its Bravais lattice consists of two atoms *A* and *B*, with primitive vectors as:

$$\mathbf{a}_1 = \left(\frac{a}{2}, \frac{\sqrt{3}a}{2} \right), \quad \mathbf{a}_2 = \left(\frac{a}{2}, -\frac{\sqrt{3}a}{2} \right) \tag{2.1}$$

where $a = |\mathbf{a}_1| = |\mathbf{a}_2|$ is the lattice constant and, in graphene, $a = 2.46$ Å [6]. In each unit cell, atom *A* and *B* are inequivalent. We denote the "A lattice" as consisting of all the *A* atoms and "*B* lattice" of *B* atoms.

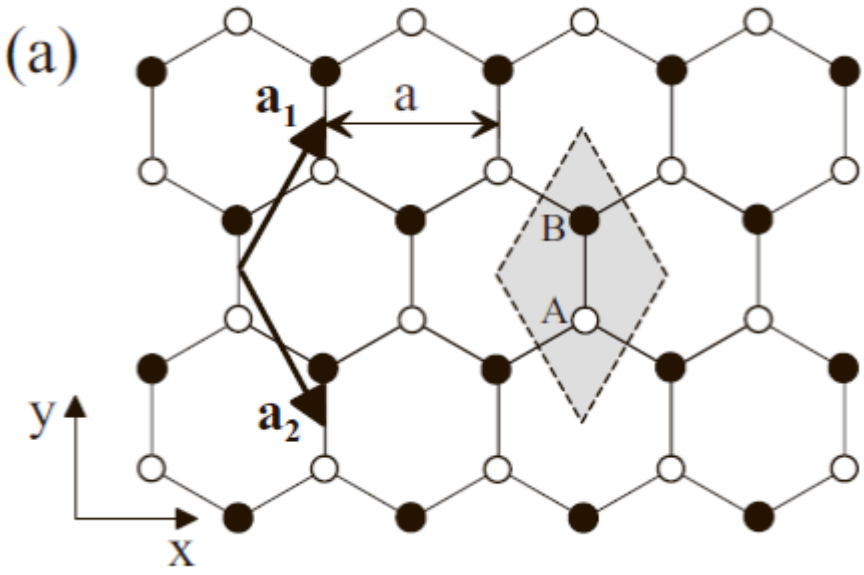

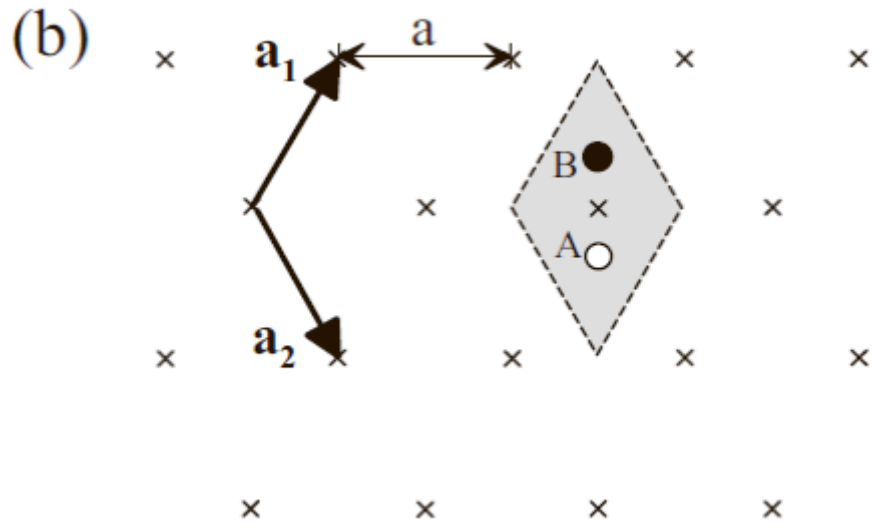

FIGURE 2.2 (a) The honeycomb crystal structure of monolayer graphene where white (black) circles indicate carbon atoms on *A* (*B*) sites and straight lines indicate σ bonds between them. Vectors $\mathbf{a}_1$ and $\mathbf{a}_2$ are primitive lattice vectors of length equal to the lattice constant a. The shaded rhombus is a unit cell containing two atoms: one *A* and one *B*. (b) Crosses indicate lattice points of the hexagonal Bravais lattice. The honeycomb structure in (a) consists of the hexagonal Bravais lattice [shown in (b)] with a basis of two atoms, one *A* and one *B*, at each lattice point. (ref. 6)

The reciprocal lattice vectors, $\mathbf{b}_1$ and $\mathbf{b}_2$, must satisfy $\mathbf{a}_1 \cdot \mathbf{b}_2 = \mathbf{a}_2 \cdot \mathbf{b}_1 = 0$ and $\mathbf{a}_1 \cdot \mathbf{b}_1 = \mathbf{a}_2 \cdot \mathbf{b}_2 = 2\pi$. Therefore we have:

$$\mathbf{b}_1 = \left(\frac{2\pi}{a}, \frac{2\pi}{\sqrt{3}a} \right), \quad \mathbf{b}_2 = \left(\frac{2\pi}{a}, -\frac{2\pi}{\sqrt{3}a} \right) \tag{2.2}$$

Assuming in one unit cell, we have n atomic orbitals ϕ_j, where j=1, 2, 3 … n, and in a lattice, the system has translational invariance, we can use n Bloch Functions $\Phi_j(\mathbf{k},\mathbf{r})$ to describe the system:

$$\Phi_j(\mathbf{k},\mathbf{r}) = \frac{1}{\sqrt{N}} \sum_{i=1}^{N} e^{i\mathbf{k}\cdot\mathbf{R}_{j,i}} \phi_j(\mathbf{r}-\mathbf{R}_{j,i}) \tag{2.3}$$

where the sum is over N different unit cells, labeled by index i = 1, 2, 3… N, $\mathbf{k}$ is the wave vector in the graphene plane and $\mathbf{R}_{j,i}$ denotes the position of the jth orbital in the ith unit cell. In graphene, for each atomic site, we only consider the $2p_z$ orbital. In each unit cell, there are two atoms denoted as A and B; therefore we have n=2 and we can use index A and B to replace 1 and 2 for the index j to simplify the expression.

For the Hamiltonian matrix $\mathbf{H}$, its the first diagonal element H_{AA} can be written as:

$$H_{AA} = \frac{1}{N} \sum_{i=1}^{N} \sum_{j=1}^{N} e^{i\mathbf{k}\cdot(\mathbf{R}_{A,j}-\mathbf{R}_{A,i})} \left\langle \phi_A(\mathbf{r}-\mathbf{R}_{A,i}) \middle| \mathbf{H} \middle| \phi_A(\mathbf{r}-\mathbf{R}_{A,i}) \right\rangle \tag{2.4}$$

By assuming the dominant contribution is from the same site, we have:

$$H_{AA} \approx \frac{1}{N} \sum_{i=1}^{N} \left\langle \phi_A(\mathbf{r}-\mathbf{R}_{A,i}) \middle| \mathbf{H} \middle| \phi_A(\mathbf{r}-\mathbf{R}_{A,i}) \right\rangle \tag{2.5}$$

Electronic states close to the Fermi level in graphene are described well by a model taking into account only the π orbital. This means the tight-binding model can include only one electron per atomic site, in a $2p_z$ orbital.[6] Since in orbital $2p_z$,

the energy is $\varepsilon_{2p} = \langle \phi_A(\mathbf{r}-\mathbf{R}_{A,i}) | \mathbf{H} | \phi_A(\mathbf{r}-\mathbf{R}_{A,i}) \rangle$ and the same holds for atoms in the B lattice. Therefore:

$$H_{AA} \approx \langle \phi_A(\mathbf{r}-\mathbf{R}_{A,i}) | \mathbf{H} | \phi_A(\mathbf{r}-\mathbf{R}_{A,i}) \rangle = \varepsilon_{2p} \tag{2.6}$$

$$H_{BB} = H_{AA} \approx \varepsilon_{2p} \tag{2.7}$$

For off diagonal elements, we have:

$$H_{AB} = \frac{1}{N} \sum_{i=1}^{N} \sum_{j=1}^{N} e^{i\mathbf{k}\cdot(\mathbf{R}_{B,j}-\mathbf{R}_{A,i})} \langle \phi_A(\mathbf{r}-\mathbf{R}_{A,i}) | \mathbf{H} | \phi_A(\mathbf{r}-\mathbf{R}_{B,i}) \rangle \tag{2.8}$$

that describes hopping between A and B lattices. Here we assume the main contribution to the hopping term is the nearest neighbor hopping. Therefore, for each atom in Lattice A, it has three neighbors in Lattice B (see Figure 2.3). Hence H_{AB} can be expressed as

$$H_{AB} \approx \frac{1}{N} \sum_{i=1}^{N} \sum_{l=1}^{3} e^{i\mathbf{k}\cdot(\mathbf{R}_{B,l}-\mathbf{R}_{A,i})} \langle \phi_A(\mathbf{r}-\mathbf{R}_{A,i}) | \mathbf{H} | \phi_A(\mathbf{r}-\mathbf{R}_{B,l}) \rangle \tag{2.9}$$

We now define $\gamma_0 = -\langle \phi_A(\mathbf{r}-\mathbf{R}_{A,i}) | \mathbf{H} | \phi_A(\mathbf{r}-\mathbf{R}_{B,l}) \rangle$ (2.10)

and: $$f(\mathbf{k}) = \sum_{l=1}^{3} e^{i\mathbf{k}\cdot\boldsymbol{\delta}_l} , \tag{2.11}$$

where $\boldsymbol{\delta}_l = \mathbf{R}_{B,l} - \mathbf{R}_{A,i}$.

Then H_{AB} can be simplified as: $H_{AB} \approx -\gamma_0 f(\mathbf{k})$ (2.12)

From Figure 2.3, the three vectors from atom A to its three neighbors are:

$$\boldsymbol{\delta}_1 = (0, \frac{a}{\sqrt{3}}), \quad \boldsymbol{\delta}_2 = (\frac{a}{2}, -\frac{a}{2\sqrt{3}}), \quad \boldsymbol{\delta}_3 = (-\frac{a}{2}, -\frac{a}{2\sqrt{3}}), \tag{2.13}$$

where $|\boldsymbol{\delta}_1| = |\boldsymbol{\delta}_2| = |\boldsymbol{\delta}_3| = a/\sqrt{3}$, which is the C-C bond length. By plugging (2.13)

into (2.11), one can get:

$$f(\mathbf{k}) = e^{ik_y a/\sqrt{3}} + e^{ik_x a/2} e^{-ik_y a/2\sqrt{3}} + e^{-ik_x a/2} e^{-ik_y a/2\sqrt{3}} = e^{ik_y a/\sqrt{3}} + 2e^{-ik_y a/2\sqrt{3}} \cos(k_x a/2)$$

(2.14)

Since H_{BA} is the conjugate of H_{AB}, we have: $H_{BA} \approx -\gamma_0 f^*(\mathbf{k})$ (2.15)

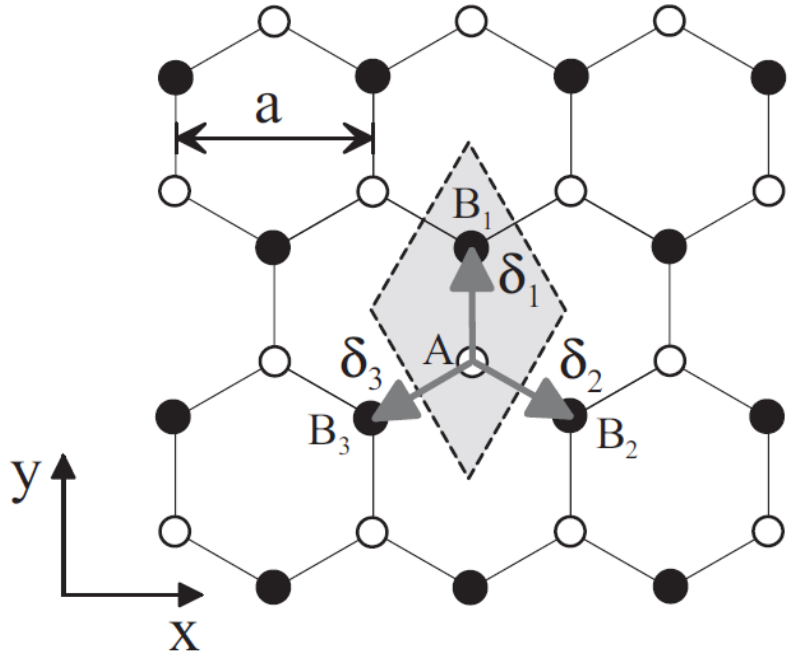

FIGURE 2.3. The honeycomb crystal structure of monolayer graphene. In the nearest neighbor approximation, we consider hopping from an *A* site (white) to three adjacent *B* sites (black), labeled B_1, B_2, B_3, with position vectors $\boldsymbol{\delta}_1$, $\boldsymbol{\delta}_2$, $\boldsymbol{\delta}_3$, respectively, relative to the *A* site.[6]

To evaluate the E_j (the energy of *j*th band), we need to calculate the overlap integral matrix $\mathbf{S}$ based on the secular equation: $\det(\mathbf{H} - E_j\mathbf{S}) = 0$. Since the

overlap between a $2p_z$ orbital on the same atom is unity, if we only count on contribution from the same atom, we can evaluate the diagonal element of overlap integral matrix as following:

$$S_{AA} = \frac{1}{N}\sum_{i=1}^{N}\sum_{j=1}^{N} e^{i\mathbf{k}\cdot(\mathbf{R}_{A,j}-\mathbf{R}_{A,i})} \left\langle \phi_A(\mathbf{r}-\mathbf{R}_{A,i}) \middle| \phi_A(\mathbf{r}-\mathbf{R}_{A,j}) \right\rangle$$

$\approx \frac{1}{N}\sum_{i=1}^{N}\left\langle \phi_A(\mathbf{r}-\mathbf{R}_{A,i}) \middle| \phi_A(\mathbf{r}-\mathbf{R}_{A,i}) \right\rangle = \frac{1}{N}\sum_{i=1}^{N} 1 = 1$. Similarly, we have $S_{BB} = S_{AA} \approx 1$.

For those off diagonal elements, we have:

$$S_{AB} \approx \frac{1}{N}\sum_{i=1}^{N}\sum_{l=1}^{3} e^{i\mathbf{k}\cdot(\mathbf{R}_{B,l}-\mathbf{R}_{A,i})} \left\langle \phi_A(\mathbf{r}-\mathbf{R}_{A,i}) \middle| \phi_A(\mathbf{r}-\mathbf{R}_{B,l}) \right\rangle = s_0 f(\mathbf{k}) \qquad (2.16)$$

and $S_{BA} \approx s_0 f^*(\mathbf{k})$. where $s_0 = \left\langle \phi_A(\mathbf{r}-\mathbf{R}_{A,i}) \middle| \phi_A(\mathbf{r}-\mathbf{R}_{B,l}) \right\rangle$.

by solving the secular equation, we can get:

$$E_{\pm} = \frac{\varepsilon_{2p} \pm \gamma_0 |f(\mathbf{k})|}{1 \mp s_0 |f(\mathbf{k})|} \quad \text{(ref. 6)} \qquad (2.17)$$

where the parameters $\gamma_0 = 3.033eV, s_0 = 0.129, \varepsilon_{2p} = 0$ are used. (ref. 6) The band structure is plotted in Figure 2.4.

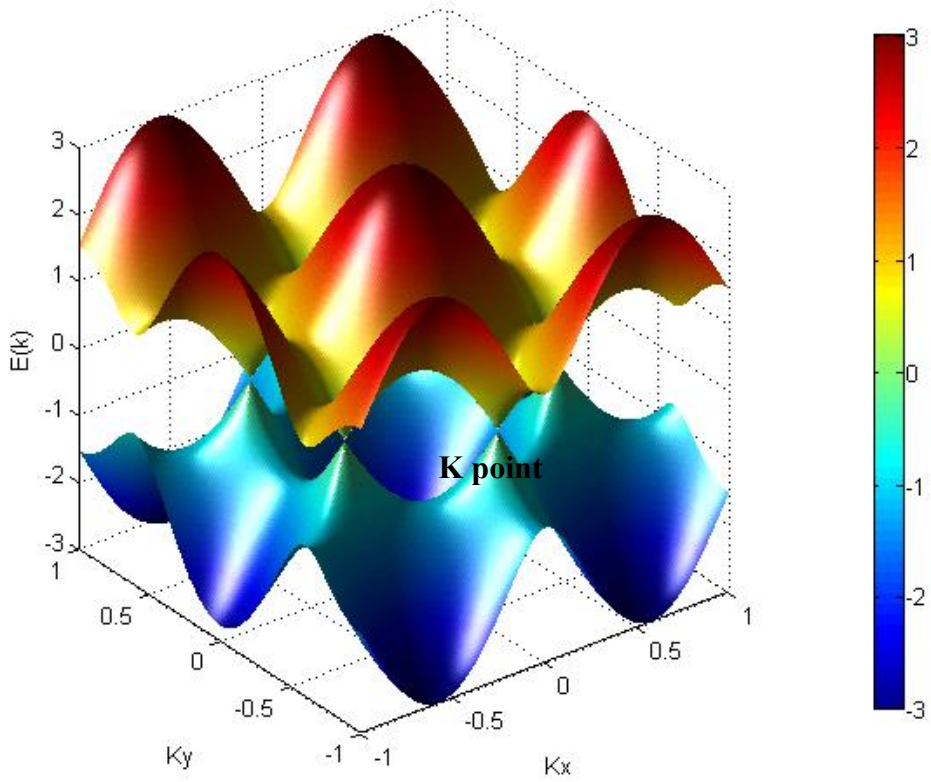

Figure 2.4. The 3-D view of band structure of single layer graphene.

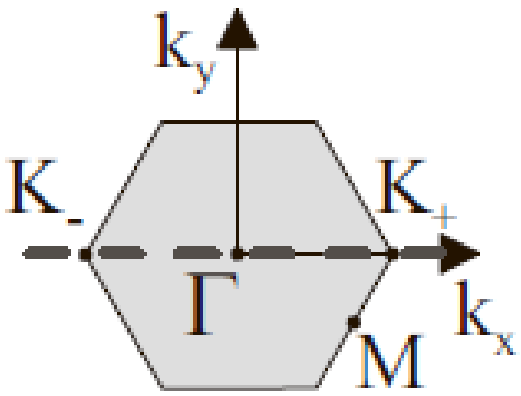

Figure 2.5 The Brillouin zone of hexagonal lattice.

From Figure 2.4 and Figure 2.5, it is obvious that single layer graphene is a gapless semiconductor and, at the K points, $E_{\pm}(\mathbf{K}) = 0$. Around the region close to K points, we have a linear dispersion relationship:

$$E_{\pm}(\mathbf{K} + \mathbf{k}) = \pm \hbar v_F \left|\mathbf{k}\right| \tag{2-18}$$

Where $v_F = 1 \times 10^6 m/s$ is the Fermi Velocity.[7] This linear dispersion relationship means that electrons behave like photons, *i.e.* massless particles, with an effective "light speed" $1 \times 10^6 m/s$ .The main difference between them is: photon is a Boson, while electrons in graphene is still Fermion with spin 1/2.

2.3 Synthesis of large scale graphene and the applications

One advantage of graphene for applications is that one can synthesis large area graphene membranes for wafer-scale (or even larger) devices, which can be achieved via two different techniques. The first method is heating up silicon carbide (SiC) to high temperatures (>1100 °C) to reduce it to graphene.[8] This process produces epitaxial graphene with dimensions as large as the size of the SiC substrate. The second approach is via chemical vapor deposition (CVD). This method takes advantage of a source gas and the atomic structure of a metal substrate to seed the growth of the graphene. The most widely used metal is Cu,

on which the graphene growth is self-limiting within certain pressure ranges. Graphene sheets as large as the underlying Cu foil (up to 30 inch in diameter) can be synthesized[9,10] These large area synthesis methods paved the way to wide applications of graphene. [11]

In 2010, researchers at IBM developed graphene transistor array with a switching rate of 100 gigahertz with epitaxial graphene wafers[12]. This speed is faster than previous results on graphene devices[13], and than that of silicon transistors with the same gate length. This breakthrough demonstrates that graphene may become the candidate material of next generation transistors by replacing Si.[12]

Furthermore, graphene has high electrical conductivity and high optical transparency, rendering it a promising candidate for transparent conducting electrodes. This type of material is in highly demand in touch screens, liquid crystal displays, organic photovoltaic cells, and organic light-emitting diodes (OLED), *etc*. In addition, graphene's mechanical strength and flexibility are much more superior than those of indium tin oxide (ITO) that is currently the most widely used material for transparent electrode applications.[14, 15] Since the total amount of indium in the earth is much less than that of gold, a cheaper alternative material for ITO would be highly desirable.

Finally, graphene may even have biomedical applications. The Chinese

Academy of Sciences showed that sheets of graphene oxide are very effective in eliminating bacteria, thus may have wide application in sterilizing medical filed..[16]

Apart from the applications mentioned above, our recent works demonstrate that modified graphene structures provide insights into physics in nanoscale systems, and may also be useful for semi-conductor industry and long term information storage.[17, 18, 19]

References:

1 Novoselov, K. S.; Geim, A. K.; Morozov, S. V.; Jiang, D.; Zhang, Y.; Dubonos, S. V.; Grigorieva, I. V.; Firsov, A. A. *Science* **2004**, *306* (5296), 666–669.

2 Landau L. D. *Phys. Z. Sowjetunion* **1937**, *11*, 26.

3 Peierls R. E. *Ann. I. H. Poincare* **1935**, *5*, 177.

4 Geim, A. K.; Novoselov, K. S. Nat Mater 2007, 6, 183.

5 P.R. Wallace, *Phys. Rev.* **1947,** *71*, 622.

6 Edward McCann NanoScience and Technology, 2012, *Part 2*, page 237-275

7 R. Saito, M.S. Dresselhaus, G. Dresselhaus Physical Properties of Carbon Nan-otubes, (*Imperial College Press, London*, **1998**)

8 Sutter, P. *Nature Materials* **2009** *8* (3), 171–2.

9 Bae, S.; Kim, H.; Lee, Y.; Xu, X.; Park, J-S; Zheng, Y.; Balakrishnan, J.; Lei, T.; Kim, H. R.; Song, Y. I.; Kim, Y-J; Kim, K. S.; Özyilmaz, B.; Ahn, J-H; Hong, B-H; Iijima, S. *Nature nanotechnology* **2010** *5* (8), 574–8.

10 Li, X.; Cai, W.; An, J.; Kim, S.; Nah, J.; Yang, D.; Piner, R.; Velamakanni, A.; Jung, I.; Tutuc, E.; Banerjee, S. K. ; Colombo, L. and Ruoff, R.S. *Science*, **2009** *324* (5932), 1312–4.

11 http://en.wikipedia.org/wiki/Graphene#Potential_applications

12 Lin, Y.-M.; Dimitrakopoulos, C.; Jenkins, K.A.; Farmer, D.B.; Chiu, H.-Y.; Grill, A.; Avouris, P. *Science*, **2010**, *327* (5966), 662

13 Lin, Y.-M.; Chiu, H.-Y.; Jenkins, K.A.; Farmer, D.B.; Avouris, P. ; Valdes-Garcia, A. *Electron Device Letters, IEEE*, **2010**, *31*(1), 68-70

14 Wang, X.; Zhi, L. and Müllen, K. *Nano Lett.*, **2007** *8* (1), 323–7

15 Eda, G.; Fanchini, G. and Chhowalla, M. *Nature Nanotechnology*, **2008** *3* (5), 270–4.

16 Hu, W.; Peng, C.; Luo, W.; Lv, M.; Li, X.; Li, D.; Huang, Q. and Fan,

C. *ACS Nano*, **2010** *4* (7), 4317–4323.

17 Zhang, H.; Bekyarova, E.; Huang, J.-W.; Zhao, Z.; Bao, W.; Wang, F.; Haddon, R. C.; Lau, C. N. *Nano Lett.* **2011**, *11*, 4047−4051.

18 Standley, B; Bao, W.; Zhang, H.; Bruck, J.; Lau, C. N.; Bockrath, M. *Nano Lett.* **2008**, *8*, 3345–3349

19 Zhang, H.; Bao, W.; Zhao, Z.; Huang, J.-W.; Standley, B.; Liu, G.; Wang, F.; Kratz, P.; Jing, L.; Bockrath, M.; Lau, C. N. *Nano Lett.* **2012**, *12*, 1772.

Chapter 3

Sample Preparation and Device Fabrication

In this chapter, I will describe in detail sample (graphene) preparation, localization and identification (See Section 3.1), and a software we developed to speed up and simplify the process of sample identification. The process of device fabrication will be discussed in Section 3.2.

3.1 Sample (graphene) preparation, localization and identification

To isolate graphene flakes from bulk graphite, we used mechanical exfoliation method with scotch tape, which was first developed by Novoselov and Geim[1]. The process of this method can be divided into the following steps:

(1) Wafer cleaning: 5mm by 5mm Si/SiO_2 wafers are selected and put into a beaker contains Acetone. Then the beaker is sonicated for ~20min. Finally, wafers are rinsed by IPA (isopropyl alcohol) and dried by N_2 gas (nitrogen).

(2) Exfoliate graphene flakes on top of SiO_2 with the method described in ref. 1.

(3) Locating samples: The dimension of our samples are typically 1μm~ 10μm.

On the Si substrate with 300nm SiO_2 , the contrast between graphene and substrate can be distinguished by naked eyes, therefore, samples are usually first located with optical microscopy method. Figure. 3.1 shows the optical image of a graphene sheet exfoliated on a Si/SiO_2 wafer.

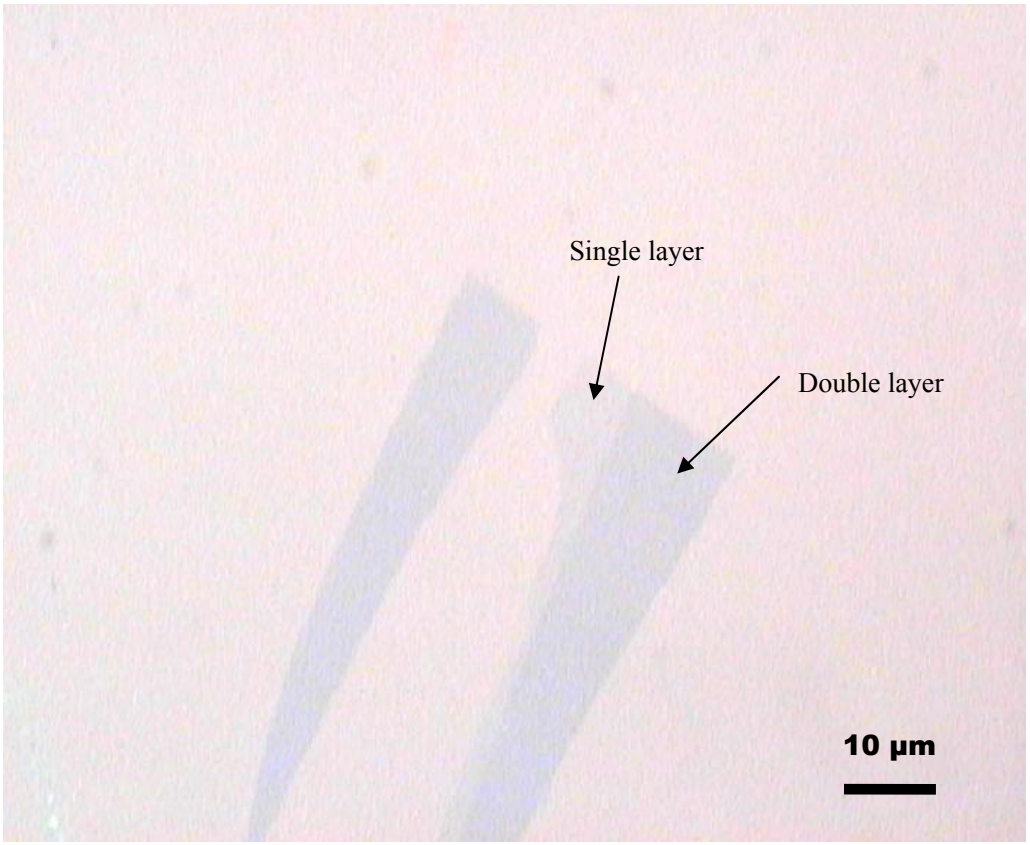

FIGURE 3.1. Optical image of Single and double layer graphene samples on top of a Si/SiO_2 wafer. The thickness of SiO_2 is 300nm. Scale bar: 10μm.

(4) Sample identification: To accurately determine the number of layers in a given

graphene sheet, one may perform Raman spectroscopy[2] or quantum Hall measurements[1,3]. However, both techniques are time consuming. Instead, the easiest and fastest method is the optical contrast between sample and the substrate. As seen in Figure 3.1, single-layer graphene appears in the upper left corner of the flake on the right, and the rest of the flake is bi-layer. The number of layers can be rather reliably identified by an experienced user. However, to take the guesswork out of this step, we develop a quantitatively analysis of the color channels (RBG data) of the sample and the substrate from an optical image file (e.g. JPG, BMP…). I have developed a software, named graphene layer viewer, for sample identification with the algorithm based on the contrast between average RGB values of sample and of the substrate area closed to the sample. (Because of the non-uniform illumination of the light source, one should select the substrate region close to the sample.) This tool can also help a novice identify samples in an efficient way.

This software and the manual can be found at https://sites.google.com/site/graphenelayer/. The latest source code of the software (written in java) is appended as Appendix I.

3.2 Device Fabrication

To measure transport properties of graphene samples, metal electrodes

attached onto samples are necessary. Generally, we use standard electron beam (e-beam) lithography (EBL) to define the pattern of electrodes in a PMMA mask, and deposit metal electrodes using an electron beam evaporator. For suspended structures, wet etching process is needed to etch away SiO_2 underneath graphene samples and/or electrodes after previous steps[4-8].

The standard fabrication process is shown in Figure 3.2 and the detailed steps are:

(1) Spin coat and bake two layers of E-beam resists: one can either choose MMA ((8.5) MMA EL 9 from Microchem) as the bottom layer and PMMA (PMMA 950 A4 from Microchem) as the top layer, or two layers of PMMA. The spin speed is 4000 RPM for 40 seconds, and baking time is 180℃ for 10 min. (Figure 3.2 a and b)

(2) Electron-beam exposure and developing: The electrodes pattern is designed with software named Design CAD LT 2000. Another tool, Nanometer Pattern Generation System (NPGS), converts designed patterns into readable files for the SEM machine (LEO SUPRA 55 Scanning Electron Microscope) in order to proceed electron beam lithography. For fine features (<2μm in scale), we use the 20μm aperture. When the beam current is set as 95pA, the typical dosage is 650 nC/cm^2. For bonding pad and larger electrodes (10μm – 250μm in scale), we use the 120μm aperture; the typical dosage is 550nC/cm^2 at a beam current of

3600pA. After electron beam exposure, our samples are developed by immersing into Methyl Isobutyl Ketone/Isopropyl Alcohol (MIBK/IPA) (1:3) solution for 65 seconds, followed by 60 seconds rinsing in IPA.

(3) Metal deposition and lift off: For alignment marks, no metal deposition and lift off process are needed, since the contrast between developed region (alignment marks) and undeveloped region in SEM is large enough for the purpose of alignment. For electrodes, we use electron-beam evaporator (Temescal BJD 1800 system) to deposit metals: 5–10nm Cr as an adhesion layer, and 100–150nm Au. The depositing rate is generally ~0.25 nm/s. The environmental vacuum inside the chamber is below 4×10^{-6} torr before starting deposition.

The lift off process removes metal deposited on the unexposed resists. We place the samples into a hot Acetone beaker (50℃~60℃) for several hours, rinse samples with IPA for ~20min and blow dry with nitrogen gas.

(4) To complete devices with suspended structure, a final wet etching step is needed. The samples are placed in a small flat plastic bowl and submerged into a beaker containing hydrofluoric acid (typically buffered oxidant etchant, or BOE) to partially or completely etch away SiO_2 underneath graphene or metal electrodes. (See Figure 3.2e) The thickness of etched SiO_2 can be controlled by adjusting etching time. Then we transfer the plastic bowl with samples and solution into beakers of DI water. This step is repeated several times to completely remove the

acid. The plastic bowl is then transferred into several IPA beakers successively to remove water. This step is important since IPA has smaller surface tension, so that the suspended structures are less prone to collapse during the drying process. The final IPA beaker is placed onto a hot plate that is heated to 80℃.Then the samples are transferred from the hot IPA onto another hot plate at 70℃. Since the high temperature decreased the surface tension of solutions, the final step helps to suspend the device. A schematic of a typical suspended device is shown in Figure 3.2f

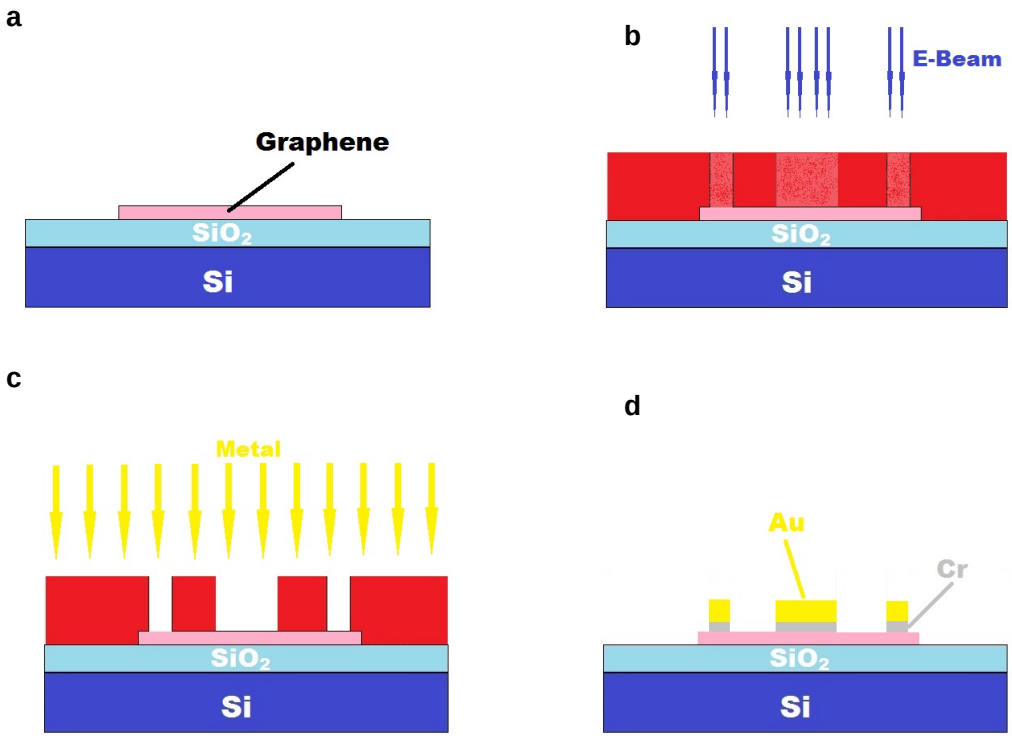

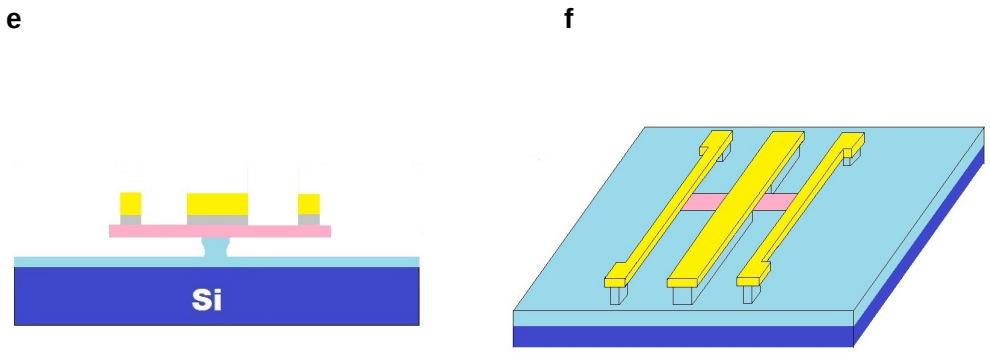

FIGURE 3.2 Device fabrication: (a) Prepare and located graphene samples on top of SiO_2/Si substrate. (b) Spin coat 2 layers of PMMA, then use electron-beam lithography to open windows for metal deposition. (c) Metals are deposited by E-beam evaporation. (d) Lift off process removed PMMA resists and metals in the non-exposed region. (e) After BOE etching, a suspended structure was finished (A profile map for center of the device). (f) Schematics of a suspended device in a 3-D view.

References:

1 Novoselov, K. S.; Geim, A. K.; Morozov, S. V.; Jiang, D.; Zhang, Y.; Dubonos, S. V.; Grigorieva, I. V.; Firsov, A. A. *Science* **2004**, *306*, 666.

2 Ferrari, A. C.; Meyer, J. C.; Scardaci, V.; Casiraghi, C.; Lazzeri, M.; Mauri, F.; Piscanec, S.; Jiang, D.; Novoselov, K. S.; Roth, S.; Geim, A. K. *Physical Review Letters* **2006**, *97*, 187401.

3 Zhang, Y.; Tan, Y.-W.; Stormer, H. L.; Kim, P. *Nature* **2005**, *438*, 201.

4 Bolotin, K. I.; Ghahari, F.; Shulman, M. D.; Stormer, H. L.; Kim, P. *Nature* **2009**, *462*, 196.

5 Du, X.; Skachko, I.; Barker, A.; Andrei, E. Y. *Nat Nanotechnol* **2008**, *3*, 491.

6 Bao, W.; Miao, F.; Chen, Z.; Zhang, H.; Jang, W.; Dames, C.; Lau, C. N. *Nat Nanotechnol* **2009**, *4*, 562.

7 Velasco, J., Jr.; Jing, L.; Bao, W.; Lee, Y.; Kratz, P.; Aji, V.; Bockrath, M.; Lau, C. N.; Varma, C.; Stillwell, R.; Smirnov, D.; Zhang, F.; Jung, J.; MacDonald, A. H. *Nat Nanotechnol* **2012**, *7*, 156.

8 Zhang, H.; Bao, W.; Zhao, Z.; Huang, J. W.; Standley, B.; Liu, G.; Wang, F.; Kratz, P.; Jing, L.; Bockrath, M.; Lau, C. N. *Nano Lett* **2012**, *12*, 1772.

Chapter 4

Aryl functionalization in single layer graphene devices

Chemical functionalization is a promising route to band gap engineering of graphene. In this chapter we focus on graphene sheets that are chemically grafted with nitrophenyl groups. Our transport measurements demonstrate that non-suspended functionalized graphene behaves as a granular metal, with variable range hopping transport and a mobility gap ~0.1 eV at low temperature. For suspended graphene that allows functionalization on both surfaces, we demonstrate tuning of its electronic properties from a granular metal to a semiconductor in which transport occurs via thermal activation over a transport gap ~80 meV from 4 to 300 K. This noninvasive and scalable functionalization technique paves the way for CMOS-compatible band gap engineering of graphene electronic devices.

I will begin this chapter by discussing previous works in this field and significance and breakthrough of our work, especially on application potential of

the chemical modification. In Section 4.2, I will describe device preparation, chemical modification process, and measurement setup. I will present detailed data analysis and transport mechanisms in non-suspended and suspended samples in Section 4.3 and 4.4, respectively. Finally, I will summarize our work.

4.1 Band Gap Engineering and Functionalized Graphene

Since its experimental isolation on insulating substrates[1] and the development of a wafer scale growth technology,[2] graphene has rapidly become a promising candidate for next generation electronic material.[3] Its material properties, such as atomically thin dimension, unparalleled room-temperature mobility,[4-8] thermal conductivity,[9] and current carrying capacity,[10] are far superior to those of silicon, whereas its two-dimensionality (2D) is naturally compatible with standard CMOS-based technologies. However, as a gapless semiconductor, graphene cannot be directly applied in standard digital electronic circuitry. Thus, in order to realize its potential to supplement or replace Si, band gap creation and control in graphene still pose a major challenge. Various approaches have been proposed and implemented, such as the use of biased bilayers, [11,12] graphene nanoribbons, [13,14] and strain-based device fabrication.[15,16] Chemical functionalization,[17-20] because of its simple implementation and potential compatibility with wafer-scale heterogeneous integration, is a particularly promising approach. Prior work in this

area includes hydrogenation to form graphane,[21,22] a wide band gap semiconductor, and fluorination to form insulators.[23-25] However, such functionalization procedures are invasive, thermally unstable, and highly energetic processes that are incompatible with standard semiconductor technology.

In this chapter, we will show the successful aryl-group functionalization[26] and transport measurements of single layer graphene sheets that are isolated in the form of free-standing films or supported on Si/SiO_2 substrates. Functionalization of graphene is verified by the development of D and D* peaks in Raman spectroscopy measurements.[27,28] The chemical treatment is simple and noninvasive and leads to the formation of stable sp3 C-C bonds to the basal plane of graphene and can be easily scaled up for industrial production. The devices' field effect mobility after functionalization is ~50 $cm^2/(V\ s)$ for substrate-supported graphene and ~200 for the suspended films, comparable with that of Si. By performing electrical measurements at different temperatures, we demonstrate that non-suspended functionalized (NSF) graphene behaves as a granular metal, displaying variable range hopping (VRH) transport, a localization-induced gap ~0.1 V at 4 K, and a charge localization length of 40~125 nm. In the case of the suspended devices which allow double-sided grafting of the aryl groups, we obtain a variable degree of functionalization, and consequently the transport mechanism spans a large range: charges traverse across

lightly functionalized devices via VRH, while heavily functionalized devices behave as gapped semiconductors, in which charges are thermally activated over a transport gap of ~80 meV from 4 to 300 K. Our results demonstrate the potential for tunable electronic properties of graphene via noninvasive solution chemistry, paving the way for wafer-scale manipulation of band gap and electronic properties of graphene.

4.2 Device Fabrication and Functionalization Process

Graphene sheets were extracted from bulk graphite using standard mechanical exfoliation techniques, and coupled to Cr/Au (10nm/150nm) electrodes via electron beam lithography. The devices are then annealed in vacuum by applying a large current[29] or using a local heater. A scanning electron microscope (SEM) image of a typical non-suspended device is shown in the Figure 4.1a inset. Immediately after fabrication, these pristine devices are electrically characterized at different temperatures. Figure 4.1a displays the current-voltage (*I-V)* characteristics of one such device NS1, which is nearly linear up to 1V. With the modulation of the gate voltage V_g, which changes the charge density induced in the graphene sheet, the devices' four terminal differential conductance G at zero bias increases approximately linearly away from the Dirac point, which is at V_D=9V, indicating a field effect mobility of

μ~2000 cm^2/Vs (Figure 4.1b). Both the *I(V)* and $G(V_g)$ curves display minimal temperature dependence, in agreement with previous experiments[4-6].

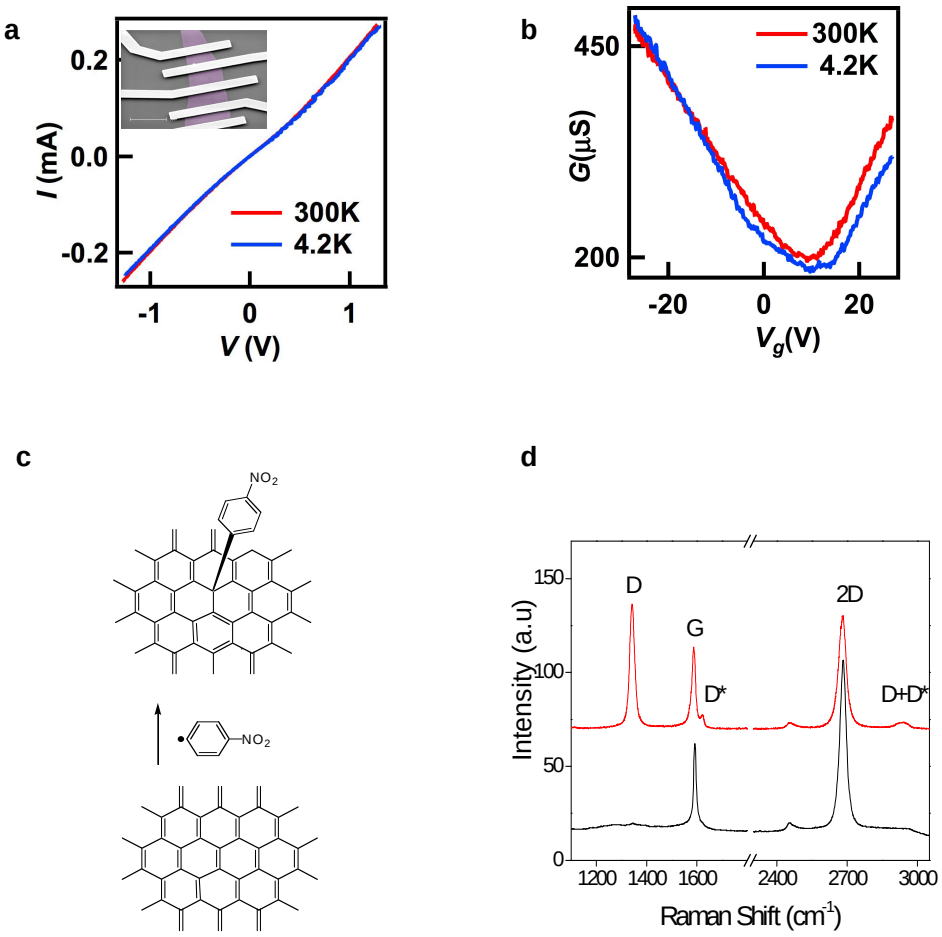

FIGURE 4.1. (a,b). *I-V* and $G(V_g)$ characteristics of a pristine graphene device NS1 on Si/SiO2 substrate at 300K (red traces) and 4K (blue traces). Inset in (a): SEM image of a device. Scale bar: 5 μm. (c). Schematics of the chemical functionalization process. (d). Raman spectrum of a graphene device before

(bottom curve) and after (top curve) functionalization.

These devices are then chemically modified by immersing in an acetonitrile solution of 4-nitrophenyl diazonium tetrafluoroborate (NO_2-$C_6H_4N_2^+BF_4^-$, 10 mM) in the presence of tetrabutylammonium hexafluorophosphate ($[Bu_4N]PF_6$, 0.1 M). The spontaneous grafting (Figure 4.1c) was performed in a glove box in the absence of light; the devices were then rinsed with acetonitrile, acetone and isopropanol and dried in air. The functionalization process was confirmed by Raman spectroscopy as discussed in previous publications[28].

Figure 4.1d shows the evolution of the Raman spectra before and after chemical attachment of aryl groups to the carbon atoms of the graphene lattice. Pristine graphene exhibits two prominent Raman peaks – a *G*-band at ~ 1580 cm^{-1} associated with the doubly degenerate phonon mode (E_{2g}) at the Brillouin zone center, and the 2*D*-band at ~2700 cm^{-1} that originates from a second order double resonance process. The intensity of the 2*D*-band relative to the *G*-band is characteristic of monolayer graphene. In some pristine graphene samples, the *G*-band was observed at 1590 cm^{-1}; such blue-shift of *G*-peak suggests *p*-doping, which is presumably due to environmental oxygen, is confirmed by transport measurements. After chemical treatment, the Raman spectra of all of the devices

developed strong *D*-bands at ~1340 cm^{-1}, accompanied by small *D**-bands at 1620 cm^{-1} and *D*+*D** bands; the reduction in intensity of the 2D band is indicative of doping of the films by the reagent[30]. The functionalized devices are stable up to more than 200 ºC.

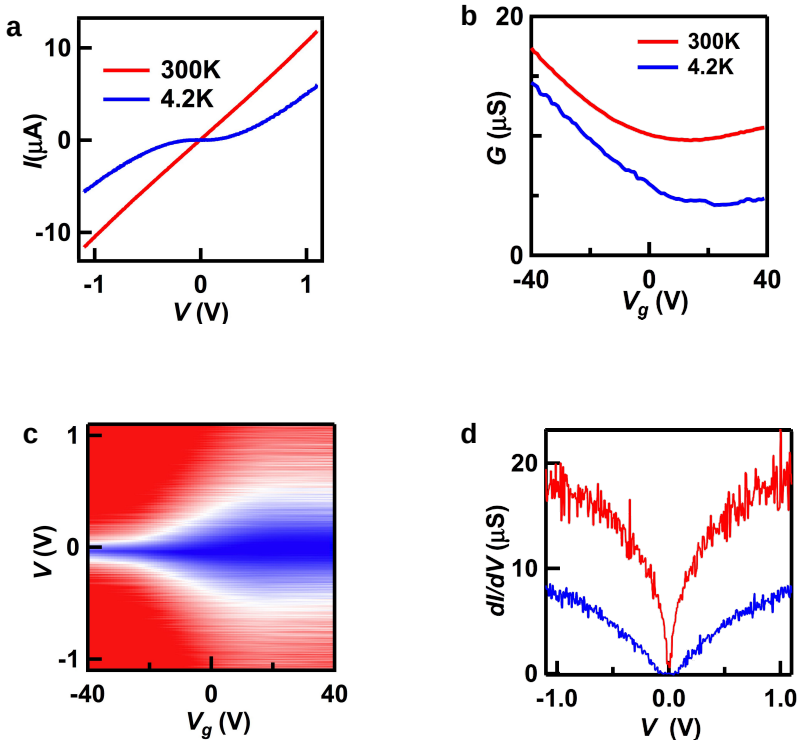

FIGURE 4.2. Transport data of NS1 after functionalization. (a,b). *I*-*V* and $G(V_g)$ characteristics. Red and blue traces are taken at 300K and 4K, respectively. (c). dI/dV (color) vs. bias *V* and V_g at *T*=4K. (d). Line traces of (c) at V_g=38V (Dirac point) and -28.5V, respectively.

After functionalization, the devices are annealed again at $T<\approx 150^{o}C$. Transport characteristics through the NSF devices are dramatically altered from those of pristine graphene. As shown by the red traces in Figure 4.2a-b, at 300K, the *I-V* curves of device NS1 are approximately linear; however, the device conductance decreases by a factor of 20 from that of pristine graphene, while μ decreases to ~ 50 cm^2/Vs. At low temperature T=4.2K, the *I-V* characteristics becomes markedly non-linear. For small bias, the conductance is effectively zero for all values of V_g; at higher bias, the $G(V_g)$ curve recovers its high temperature behavior, albeit with ~20% reduction in conductance. We note that at 4K, the Dirac point shifts to 38V, presumably due to random charge fluctuations in the electromagnetic environment of the device.

At low temperature, the most notable feature of the device's behavior is the zero or extremely small conductance at small bias. Figure 4.2c displays the differential conductance dI/dV of the device (color), which is obtained by numerically differentiating the *I-V* curves taken at different V_g value, as functions of V_g (horizontal axis) and V (vertical axis). Two line traces, dI/dV vs. V at the Dirac point V_g=38V and at the highly hole-doped regime V_g=-28.5V, are shown in Figure 4.2d. The blue region, which has effectively zero conductance (<0.1 μS), appears as a half diamond. Similar diamond-shaped low G regions have been observed in extremely narrow graphene nanoribbons[14], and suggests the formation

of a transport gap or mobility gap at low temperature. From the height of region with dI/dV<0.1 μS in Figure 4.2c, we estimate the magnitude of the transport gap to be ~0.1 eV.

4.3 Mechanisms of Transport properties

In order to elucidate the transport mechanism of the device, we investigated the temperature dependence of its *I-V* characteristics. For transport across a true band gap Δ, one expects thermally activated behavior, $G \propto e^{-\Delta/2k_BT}$, where k_B is Boltzmann constant. Figure 4.3a displays the *I-V* characteristics of device NS1 taken at different temperatures between 14 K and 300K, which exhibits a transition from non-linear to linear *IV* as *T* increases. The low bias conductance *G* in the linear response regime is extracted and plotted in Figure 4.3b as a function of 1/*T*, where the red and green data points corresponding to those taken at the Dirac point and at highly electron-doped regime, respectively. The non-linearity of the data excludes thermal activation as the transport mechanism.

Another possible mechanism is variable range hopping (VRH)[31-33], in which the electrons in a strongly disordered or granular system traverse the system via a series of hops to neighboring localized states. The hopping distance is determined by a competition that maximizes the wave function overlap and minimizes the activation energy between the two sites. As a result, the zero bias conductance has

a stretched-exponential dependence on T

$$G = A\exp\left[-\left(\frac{T_0}{T}\right)^{\alpha}\right] \qquad (1)$$

where A and T_0 are constants. The exponent α, which depends on the dimensionality and anisotropy of the system, strength of disorder and dielectric constant, has been theoretically and experimentally determined to vary from ¼ to 3/4 in systems as varied as carbon nanotube networks[34], polymers[35], arrays of nanoparticles[36, 37] and the 2D electron gas in the quantum Hall regime[38]. Generally, there exist two different VRH regimes. In the Mott VRH regime[32], the system has a constant density of states (DOS) near the Fermi level, and negligible Coulomb interaction between the hopping sites. This regime dominates at high temperature, yielding α=1/(d+1), where d is the dimensionality of the system. At sufficiently low temperatures, Coulomb interaction between the sites gives rise to a Coulomb gap at the Fermi level; in this Efros-Shklovskii (ES) regime, α=1/2 for all d[31]. Since d=2 for graphene, we expect α=1/3 in the Mott regime and α=1/2 in the ES regime. The ES VRH model also applies for granular metals[39, 40], where transport occurs via multiple electron co-tunneling among different grains[40].

To quantitatively account for our results, we fit the data in Figure 4.3b to Eq. (1), as shown by the solid lines in Figure 4.3b. Excellent agreement with data over the entire T range was obtained – for the data set at the Dirac point, the best-fit

parameters are A=86.9, T_0=1670K and α=0.39; for the data set at highly doped regime, A=42.2, T_0=317K and α=0.42. For both regimes, α is determined to be ~ 0.4, which may indicate a crossover from the Mott to ES VRH regimes; alternatively, it could suggest that the DOS $g(\varepsilon) \sim \varepsilon^{1/2}$ for functionalized graphene[33], where ε is the energy measured relative to the Fermi level. Further experimental and theoretical investigation of functionalized graphene will be necessary to ascertain the exponent and understand the rich underlying physics.

At low temperatures the system is expected to be in the ES regime; as shown in Figure 4.3c, the data points in the range T=14-150K fall on a straight line in the log plot of G against $T^{1/2}$ (adequate but slightly more non-linear traces are obtained if we plot against $T^{1/3}$). The data are well fit by the function $G = A\exp\left(-\sqrt{T_0/T}\right)$, with a T_0 value of 450K and 150K in the DP and highly doped regime, respectively. Since T_0 is related to electron localization length ξ[31],

$$k_B T_0 \approx C\frac{e^2}{4\pi\varepsilon_0\varepsilon_r\xi}, \qquad (2)$$

we infer ξ≈42 nm at the DP and in the doped regime, ξ≈125 nm. Here e is electron charge, ε_0 and ε_r≈2.5 are the permittivity of vacuum and of the electromagnetic environment of the device, respectively, and C~2.8 is a constant.

To check the self-consistency of the model, we also estimate the size of the

Coulomb gap Δ_C and the onset temperature T^* of the ES regime. In 2D, $\Delta_C \sim \frac{e^4 g_0}{(4\pi\varepsilon_0\varepsilon_r)^2}$, $k_B T^* \sim \frac{e^6}{(4\pi\varepsilon_0\varepsilon_r)^3} g_0^2 \xi$, where g_0 is the "bare" DOS at the Fermi level. We note that these expressions contain unknown prefactors of order unity, which need to be determined by computer simulations. g_0 for our devices are not known, but we can obtain an order-of-magnitude estimate by using graphene's DOS at charge density $n \sim 5x10^{11}$ cm^{-2}, which is the typical doping level induced by impurities. Given $g_0 = 2\sqrt{\frac{n}{\pi}} \frac{1}{\hbar v_F}$, where $v_F \sim 10^6$ m/s is the Fermi velocity, we find that $\Delta_C \sim 500$ K, which is consistent with our observation of a transport gap ~100 meV, and $T^* \sim 3000$K. Considering the uncertainties in the prefactors and g_0, these values are indeed reasonable, and also consistent with those found in other 2D systems[41, 42].

The agreement between our data and VRH model, together with the relatively small localization length, suggest that at low temperature, aryl-functionalized graphene behaves as a granular metal. Thus, the NSF device can be modeled as a 2D array of metallic islands; theoretical predictions for such a system[43] suggest that at low temperature, disorder and charging effects lead to a conduction threshold V_t, below which $G=0$. At large bias $V>V_t$, the charges percolate through the array via multiple branching paths which optimize the total charging energy, giving rise to a current with a power-law dependence on the reduced voltage

$$I \sim (V - V_t)^{\gamma} \qquad (3)$$

where γ is predicted to be 5/3 for a 2D array and the threshold voltage V_t is expected to decrease linearly with increasing T[43]. For a given system, Eq. (3) is expected to be universal at low temperatures.

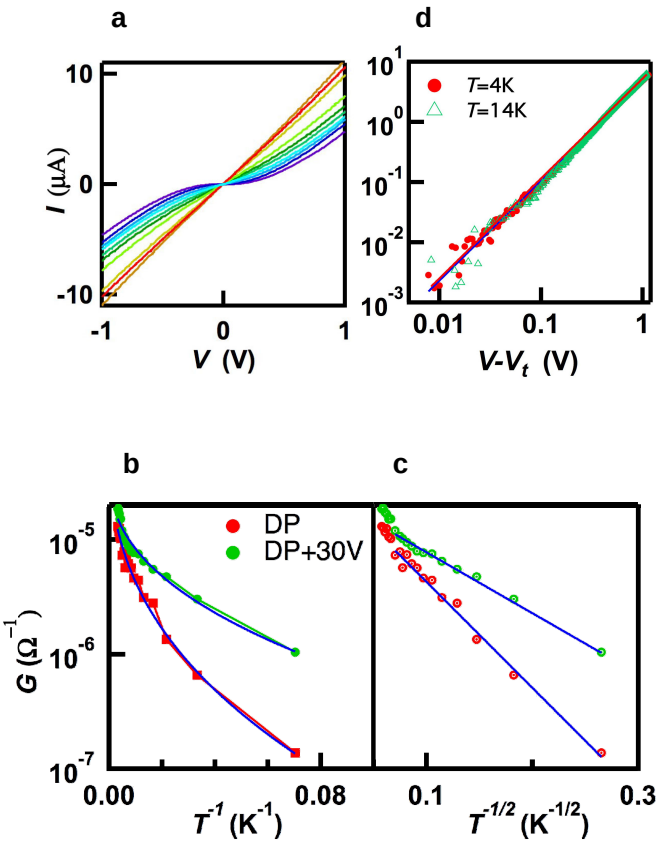

FIGURE 4.3. T-dependent transport data of NS1. (a). *I-V* curves of functionalized NS1 at *T*=14, 30, 60, 90, 120, 150, 178, 227, 257 and 283K. The data are taken at the Dirac point. (b). Linear response *G* vs. *1/T* for data taken at the Dirac point (red dots) and highly doped regimes (green dots). The solid lines are best-fitted

curves to Eq. (1). Data at T=4K and 14K are not shown, since the measured G $<10^{-8}\ \Omega^{-1}$ is limited by the instrument noise floor. (c). The same data points in (b), plotted as G vs. $T^{-1/2}$. The solid lines are curves fitted to Eq. (1) with α=1/2. (d). I vs. reduced voltage V-V_t for data taken at the Dirac point and T=4K and 14K, which collapse into a single curve. The red and green lines (indistinguishable) are best fits to Eq. (3), with exponent γ=1.6.

In Figure 4.3d, we plot I *vs.* V-V_t at T=4K and 14K; the data are taken at the DP, and V_t is chosen to be 80mV and 55mV, respectively. On the log-log plot, both curves collapse into a single straight line, indicating a power-law behavior. The best-fit exponent γ is found to be 1.66, in excellent agreement with the theoretical value of 1.6. This establishes that aryl-grafted graphene is a granular metal, with a localization induced transport gap ~ 100mV at T=4K. Furthermore, since disordered arrays often display IV characteristics that have a variety of γ values, and sometimes even deviate from the simple power law behavior[37, 44], the excellent fit of Eq. (3) to the data suggests that the grafting sites are relatively well-ordered.

4.4 Suspended Samples

Finally, we focus on transport in chemically functionalized free-standing

graphene membranes. Since both sides of these membranes are exposed to the aryl solution, we expect more effective grafting due to the minimization of incommensurate ordering and relaxation of strains that result from the sp^2-to-sp^3 conversion. Moreover, functionalization of suspended graphene is critical for chemical and biological sensors based on graphene nanomechanical resonators, which promise to be highly sensitive as well as selective.

To this end, we functionalized suspended graphene devices obtained by acid release of the underlying SiO_2 layer [7, 8](Figure 4.4a). As described in Chapter 3, our sample with Au/Cr (150nm/10nm) electrodes was first prepared on 300nm SiO_2 substrate with traditional E-Beam Lithography. Cr was adopted as the sticking layer because it is stable in the BOE etching solution. Then the whole device was immersed into BOE (Buffered Oxide Etch) solution for 70s (etching away ~120nm SiO_2) or 90s (etching away ~150nm SiO_2). The sample was washed by transferring from BOE to water beakers and finally IPA (Isopropanol) beakers. The last IPA beaker should be heated up to 70~80℃, in order to minimize the surface tension, which may collapse the fragile suspended structure. Finally, we dried the device by placing it on a hot plate at ~70℃. The device was then chemically functionalized as described in the previous section, and the same rinsing and drying process was repeated.

The mobility of a typical pristine suspended device is ~5,000 to 15,000

cm^2/Vs at room temperature (Figure 4.4b). After chemical treatment, the device mobility decreases significantly, to ~ 1-200 cm^2/Vs. A lightly functionalized suspended graphene sample displays similar VRH transport characteristics to those of the NSF devices. In contrast, transport across a heavily functionalized suspended device is dramatically different. Figure 4.4c-d display the electrical characteristics of a device after 20 hours of functionalization. Its *I-V* curves are non-linear even at 300K; at 4K, the conductance is effectively zero (< 0.01 nS) for $V<1V$ (Figure 4.4c). Its zero bias conductance decreases exponentially with $1/T$ at high temperature, and crosses over to a constant value for $T<30K$ (Figure 4.4d). The data can be satisfactorily described by the equation $G(T)=G_0+Aexp(-E_A/k_BT)$, where $E_A \approx 39 \pm 10$ meV is the activation energy and G_0 is the constant background conductance, which is likely the noise floor of this measurement setup. This activation energy may arise from the formation of a true band gap – in fact, our previous study using ARPES measurement has shown the presence of a band gap of ~ 360 meV[28]; alternatively, the Arrhenious behavior may arise from nearest neighbour hopping. Thus, we demonstrate the formation of a gap $2E_A$ ~80 meV at room temperature in graphene sheets that are functionalized on both surfaces, though further experimental work will be necessary to ascertain the nature and magnitude of the gap.

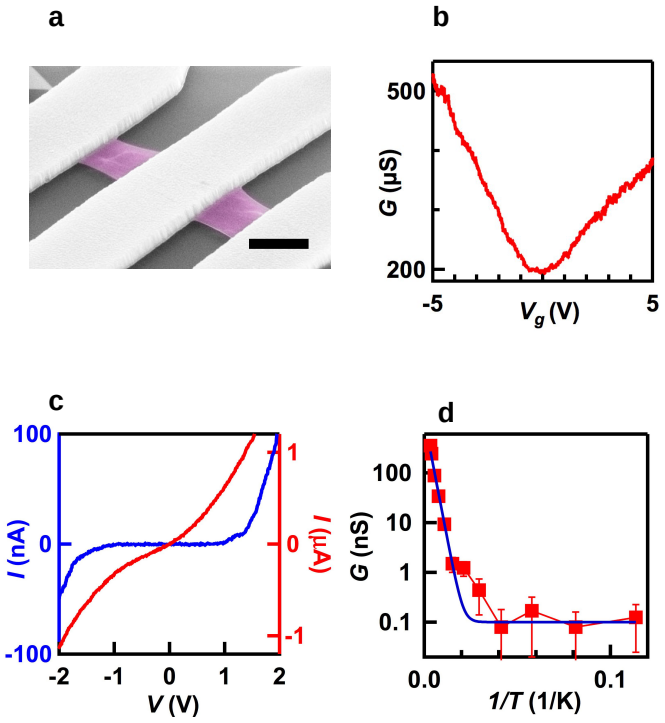

FIGURE 4.4. (a). False-color SEM image of a suspended graphene device. (b). $G(V_g)$ of a typical suspended device before functionalization. Scale bar: 1 μm. (c). *I-V* curves of a suspended functionalized device at V_g=0 and T=300K (red curve, right axis) and 4K (blue curve, left axis), respectively. (d). Linear response G *vs.* $1/T$. The solid line is the best-fit to $G(T)=G_0+Aexp(-E_A/k_BT)$, where E_A ~40 mV.

In conclusion, we have demonstrated single- and double-sided chemical functionalization of graphene sheets via grafting of aryl groups using simple solution chemistry. Via control of the functionalization, graphene can be tuned from a gapless semi-metal to granular metal with a Coulomb-induced transport

gap at low temperature, and to a semiconductor with a transport gap ~100 meV. Since the aryl-grafting technique is non-invasive and compatible with CMOS technologies, our results have significant impact for band gap engineering and control in graphene electronics.

References:

1 Novoselov, K. S.; Geim, A. K.; Morozov, S. V.; Jiang, D.; Zhang, Y.; Dubonos, S. V.; Grigorieva, I. V.; Firsov, A. A. *Science* **2004,** 306, (5296), 666-669.

2 Berger, C.; Song, Z. M.; Li, X. B.; Wu, X. S.; Brown, N.; Naud, C.; Mayo, D.; Li, T. B.; Hass, J.; Marchenkov, A. N.; Conrad, E. H.; First, P. N.; de Heer, W. A. *Science* **2006,** 312, (5777), 1191-1196.

3 Fuhrer, M. S.; Lau, C. N.; MacDonald, A. H. *MRS Bulletin* **2010,** 35, (4), 289-295.

4 Novoselov, K. S.; Geim, A. K.; Morozov, S. V.; Jiang, D.; Katsnelson, M. I.; Grigorieva, I. V.; Dubonos, S. V.; Firsov, A. A. *Nature* **2005,** 438, (7065), 197-200.

5 Zhang, Y. B.; Tan, Y. W.; Stormer, H. L.; Kim, P. *Nature* **2005,** 438, (7065), 201-204.

6 Chen, J. H.; Jang, C.; Xiao, S. D.; Ishigami, M.; Fuhrer, M. S. *Nat. Nanotechnol.* **2008,** 3, (4), 206-209.

7 Bolotin, K. I.; Sikes, K. J.; Jiang, Z.; Klima, M.; Fudenberg, G.; Hone, J.; Kim, P.; Stormer, H. L. *Sol. State Commun.* **2008,** 146, (9-10), 351-355.

8 Du, X.; Skachko, I.; Barker, A.; Andrei, E. Y. *Nat. Nanotechnol.* **2008,** 3,

(8), 491-495.

9 Balandin, A. A.; Ghosh, S.; Bao, W.; Calizo, I.; Teweldebrhan, D.; Miao, F.; Lau, C. N. *Nano Lett.* **2008,** 8, 902.

10 Standley, B.; Bao, W.; Zhang, H.; Bruck, J.; Lau, C. N.; Bockrath, M. *Nano Lett.* **2008,** 8, 3345.

11 McCann, E. *Phys. Rev. B* **2006,** 74, 161403.

12 Castro, E. V.; Novoselov, K. S.; Morozov, S. V.; Peres, N. M. R.; Dos Santos, J.; Nilsson, J.; Guinea, F.; Geim, A. K.; Castro Neto, A. H. *Phys. Rev. Lett.* **2007,** 99, (21), 216802.

13 Chen, Z.; Lin, Y. M.; Rooks, M. J.; Avouris, P. *Physica E* **2007,** 40, (2), 228--232.

14 Han, M. Y.; O, z. B.; Zhang, Y.; Kim, P. *Phys. Rev. Lett.* **2007,** 98, (20), 206805.

15 Pereira, V. M.; Castro Neto, A. H. *Phys. Rev. Lett.* **2008,** 103, 046801.

16 Bao, W. Z.; Miao, F.; Chen, Z.; Zhang, H.; Jang, W. Y.; Dames, C.; Lau, C. N. *Nat. Nanotechnol.* **2009,** 4, (9), 562.

17 Boukhvalov, D. W.; Katsnelson, M. I. *Phys. Rev. B* **2008,** 78, 085413.

18 Kaiser, A. B.; Gómez-Navarro, C.; Sundaram, R. S.; Burghard, M.; Kern, K. *Nano Lett.* **2009,** 9, (5), 1787.

19 J. Moser, H. T., S. Roche, F. Alzina, C. M. Sotomayor Torres, and A.

Bachtold. *Phys. Rev. B* **2010,** 81, (20), 205445.

20 Hong, X.; Cheng, S.-H.; Herding, C.; Zhu, J. *Phys. Rev. B* **2011,** 83, (8), 085410.

21 Elias, D. C.; Nair, R. R.; Mohiuddin, T. M. G.; Morozov, S. V.; Blake, P.; Halsall, M. P.; Ferrari, A. C.; Boukhvalov, D. W.; Katsnelson, M. I.; Geim, A. K.; Novoselov, K. S. *Science* **2009,** 323, 610-613.

22 Sofo, J. O.; Chaudhari, A. S.; Barber, G. D. *Phys. Rev. B* **2007,** 75, 153401.

23 Cheng, S. H.; Zou, K.; Okino, F.; Gutierrez, H. R.; Gupta, A.; Shen, N.; Eklund, P. C.; Sofo, J. O.; Zhu, J. *Phys. Rev. B* **2010,** 81, (20), 205435.

24 Withers, F.; Dubois, M.; Savchenko, A. K. *Phys. Rev. B* **2010,** 82, (7), 073403.

25 Xiang, H. J.; Kan, E. J.; Wei, S. H.; Gong, X. G.; Whangbo, M. H. *Phys. Rev. B* **2010,** 82, (16), 165425.

26 Bekyarova, E.; Itkis, M. E.; Ramesh, P.; Berger, C.; Sprinkle, M.; de Heer, W. A.; Haddon, R. C. *J. Am. Chem. Soc.* **2009,** 131, (4), 1336-+.

27 Ferrari, A. C.; Meyer, J. C.; Scardaci, V.; Casiraghi, C.; Lazzeri, M.; Mauri, F.; Piscanec, S.; Jiang, D.; Novoselov, K. S.; Roth, S.; Geim, A. K. *Phys. Rev. Lett.* **2006,** 97, (18), 187401.

28 Niyogi, S.; Bekyarova, E.; Itkis, M. E.; Zhang, H.; Shepperd, K.; Hicks, J.; Sprinkle, M.; Berger, C.; Lau, C. N.; Deheer, W. A.; Conrad, E. H.;

Haddon, R. C. *Nano Lett.* **2010,** 10, (10), 4061-4066.

29 Moser, J.; Barreiro, A.; Bachtold, A. *Appl. Phys. Lett.* **2007,** 91, 163513.

30 Farmer, D. B.; Golizadeh-Mojarad, R.; Perebeinos, V.; Lin, Y.-M.; Tulevski, G. S.; Tsang, J. C.; Avouris, P. *Nano Lett.* **2009,** 9, 388.

31 Efros, A. L.; Shklovskii, B. I. *J. Phys. C* **1975,** 8, (4), L49-L51.

32 Ambegaokar, V.; Halperin, B. I.; Langer, J. S. *Phys. Rev. B* **1971,** 4, (8), 2612-+.

33 Fogler, M. M.; Teber, S.; Shklovskii, B. I. *Phys. Rev. B* **2004,** 69, (3), 035413.

34 Long, Y.; Chen, Z. J.; Wang, N. L.; Ma, Y. J.; Zhang, Z.; Zhang, L. J.; Wan, M. X. *Appl. Phys. Lett.* **2003,** 83, (9), 1863-1865.

35 Brown, A. R.; Jarrett, C. P.; deLeeuw, D. M.; Matters, M. *Synthetic Metals* **1997,** 88, (1), 37-55.

36 Rimberg, A. J.; Ho, T. R.; Clarke, J. *Phys. Rev. Lett.* **1995,** 74, (23), 4714-4717.

37 Parthasarathy, R.; Lin, X. M.; Jaeger, H. M. *Phys. Rev. Lett.* **2001,** 87, (18), 186807.

38 Polyakov, D. G.; Shklovskii, B. I. *Phys. Rev. Lett.* **1993,** 70, (24), 3796-3799.

39 Zhang, J.; Shklovskii, B. I. *Phys. Rev. B* **2004,** 70, 115317.

40 Beloborodov, I. S.; Lopatin, A. V.; Vinokur, V. M.; Efetov, K. B. *Rev. Mod. Phys.* **2007,** 79, (2), 469-518.

41 Fung, A. W. P.; Wang, Z. H.; Dresselhaus, M. S.; Dresselhaus, G.; Pekala, R. W.; Endo, M. *Phys. Rev. B* **1994,** 49, (24), 17325.

42 Tran, T. B.; Beloborodov, I. S.; Lin, X. M.; Bigioni, T. P.; Vinokur, V. M.; Jaeger, H. M. *Phys. Rev. Lett.* **2005,** 95, (7), 076806.

43 Middleton, A. A.; Wingreen, N. S. *Phys. Rev. Lett.* **1993,** 71, 3198.

44 Parthasarathy, R.; Xiao-Min, L.; Elteto, K.; Rosenbaum, T. F.; Jaeger, H. M. *Phys. Rev. Lett.* **2004,** 92, (7), 076801.

Chapter 5

Organometallic Hexahapto Functionalization of Single Layer Graphene Devices

Apart from the Aryl group functionalization method, we also adopt other chemical approaches to functionalize pristine graphene samples. In this chapter, I will discuss a gentler chemical modification -- organometallic hexahapto functionalization, which provides a good compromise between the often conflicting goals of achieving both high ON-OFF ratio and maintaining the high mobility of graphene devices.

In Section 5.1, I will introduce the motivation behind this approach, the chemical treatment process and chemical properties of functionalized graphene. Detailed setup of the experiment, apparatus and parameters are described in Section 5.2. Section 5.3 discusses the transport properties of devices that are functionalized to various degrees. Finally, Section 5.4 summarizes this work.

5.1 Organometallic Hexahapto Functionalization

Pristine single layer graphene (SLG) has exceedingly high mobility, which is ~4,000–20,000 cm^2/Vs for typical devices supported on Si/SiO_2 substrates, and may reach as high as 250,000 cm^2/Vs in suspended devices at room temperature.[1] Such high mobilities makes graphene an extremely attractive candidate for next generation electronic materials. However, the absence of a band gap that is necessary for digital electronics presents a technological challenge. One effective approach to band gap engineering is the (partial) saturation of the valences of some of the conjugated carbon atoms.[2-16] Nitrophenyl functionalization, in which a fully rehybridized sp^3 carbon atom is created in the lattice, dramatically modifies the electronic and magnetic structure of graphene, with significantly reduced field effect mobility.[17-21] Since this type of functionalization scheme introduces resonant scatters[22] into the graphene lattice, we refer to this as destructive rehybridization.[23]

Most approaches for chemical modification of graphene involve the creation of sp^3 carbon centers at the cost of conjugated sp^2 carbon atoms in the graphene lattice. We have recently investigated the application of organometallic chemistry by studying the covalent modification of graphitic surfaces with hexahapto zero-valent transition metals such as chromium.[12,24] The formation of the hexahapto (η^6)-arene metal bond brings about very little structural reorganization of the π-system; in the reaction of the zero-valent chromium metal with graphene,

the vacant d_π orbital of the metal (chromium) constructively overlaps with the occupied π-orbitals of graphene, without removing any of the sp^2 carbon atoms from conjugation.[12,24] Previously we have shown that the formation of such bis-hexahapto transition metal bonds between the conjugated surfaces of the benzenoid ring systems present in the surfaces of graphene and carbon nanotubes can dramatically change their electrical properties.[12,23-26] These prior works focus on using the bis-hexahapto-metal bond as an interconnect for electrical transport between the conjugated surfaces, thereby increasing the dimensionality of the carbon nanotube and graphene materials and thus we were concerned with the use of the bis-hexahapto-metal bond as a conduit for electron transport between surfaces. In contrast, the goal of the present study is to investigate the effect of the hexahapto-bonded chromium atoms on the electronic properties of graphene itself (within the plane of a single layer), by using mono-hexahapto-metal bonds to the graphene surface.

Single layer graphene (SLG) flakes are extracted from bulk graphite using a standard mechanical exfoliation method and placed on a Si substrate with 300 nm SiO_2. Contacts consisting of 10 nm of Cr and 150 nm of Au are deposited on SLG by standard e-beam lithography. The devices are annealed in vacuum by passing a high current for a short time to remove contaminants from the surface.[27] After characterization the devices are immersed in a chromium hexacarbonyl solution

for organometallic functionalization.

Three different functionalization approaches are employed to chemically modify the graphene flakes as shown in Figure 5.1. In the first method (method ***A***), SLG devices are functionalized in a solution of chromium hexacarbonyl [$Cr(CO)_6$] in dibutyl ether/tetrahydrofuran under refluxing conditions (140 ^oC, 48 h). In the second method (method ***B***), the SLG devices were immersed in a solution of $Cr(CO)_6$ as in method ***A***, but in presence of an additional ligand, naphthalene (80 ^oC for 12 h). The naphthalene was added in order to form the (naphthalene)$Cr(CO)_3$ complex,[28-30] which is known to be a very effective reagent for the transfer of the $Cr(CO)_3$ group between ligands. In our experience there is a facile arene exchange reaction between naphthalene and the more reactive graphene layer, which allows the reaction to proceed at relatively low temperature. In the third method (method ***C***), the SLG device is functionalized using a solution of tris(acetonitrile) tricarbonylchromium(0) [$Cr(CO)_3(CH_3CN)_3$][30-33] in THF (40 ^oC, 6 h).

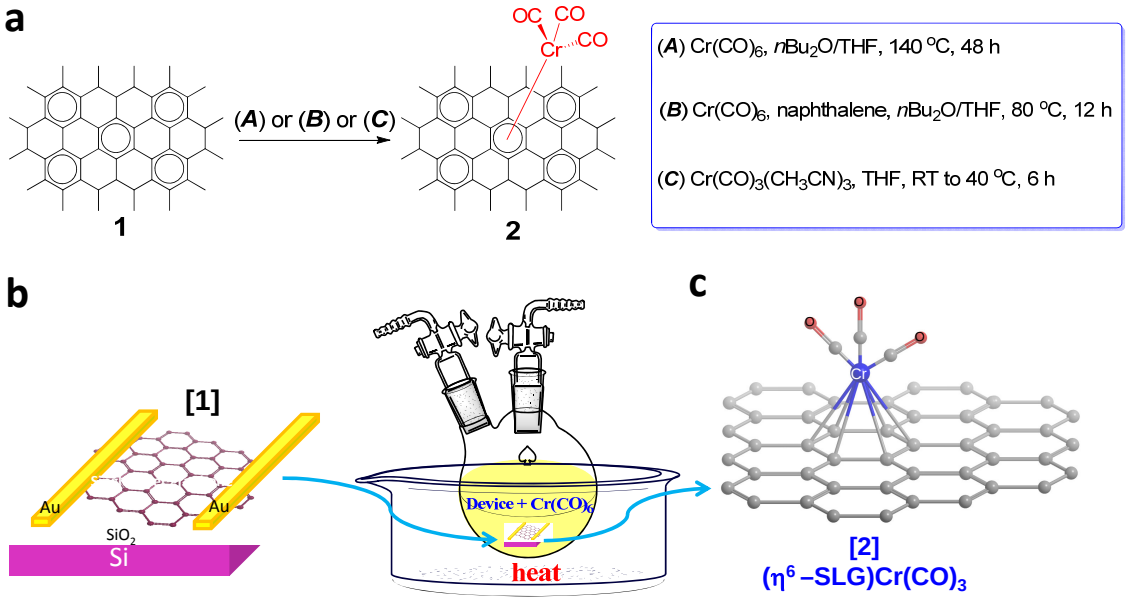

FIGURE 5.1. Organometallic functionalization of single-layer graphene devices (SLG, **1**): (a) Schematics of functionalization approaches using three different reaction routes to obtain hexahapto-chromium complex, (η^6-SLG)$Cr(CO)_3$ (**2**); routes: ***A***: $Cr(CO)_6$, *n*-Bu_2O/THF, 140 °C, 48 h, under argon, ***B***: $Cr(CO)_6$, naphthalene, *n*-Bu_2O/THF, 80 °C, 12 h, under argon, and ***C***: $Cr(CO)_3(CH_3CN)_3$, THF, room temperature to 40 °C, 6 h, under argon. (b) Illustration of the graphene device and the functionalization process; and (c) Three-dimensional model of the (η^6-SLG)$Cr(CO)_3$ organometallic complex.

To probe the effectiveness of the functionalization approaches the graphene sheets were characterized with Raman spectroscopy before and after the reaction

(λ_{ex} = 532 nm, Nicolet Almega XR). The Raman spectra of the pristine single layer graphene (SLG, Figure 5.2a-i) show the characteristic *G*-band (1585 cm^{-1}) and 2D-band (2680 cm^{-1}), while organometallic covalent hexahapto (η^6-) functionalization leads to development of a D-band located at ~1345 cm^{-1} with a relatively low intensity (Figure 5.2a, ii-iv). The Raman measurements showed that all three methods were effective in the formation of Cr-complexed graphene, although method ***C*** was found to provide functionalized graphene flakes with slightly weaker D-band intensity, which may be due to a lower degree of hexahapto (η^6-) complexation. We also observe that the reactivity of the flakes towards hexahapto organometallic functionalization reaction was dependent on the number of graphene layers; analysis of the integrated I_D/I_G ratios indicated that single-layer graphene (SLG) was more reactive than few-layer graphene (FLG) and HOPG was least reactive.

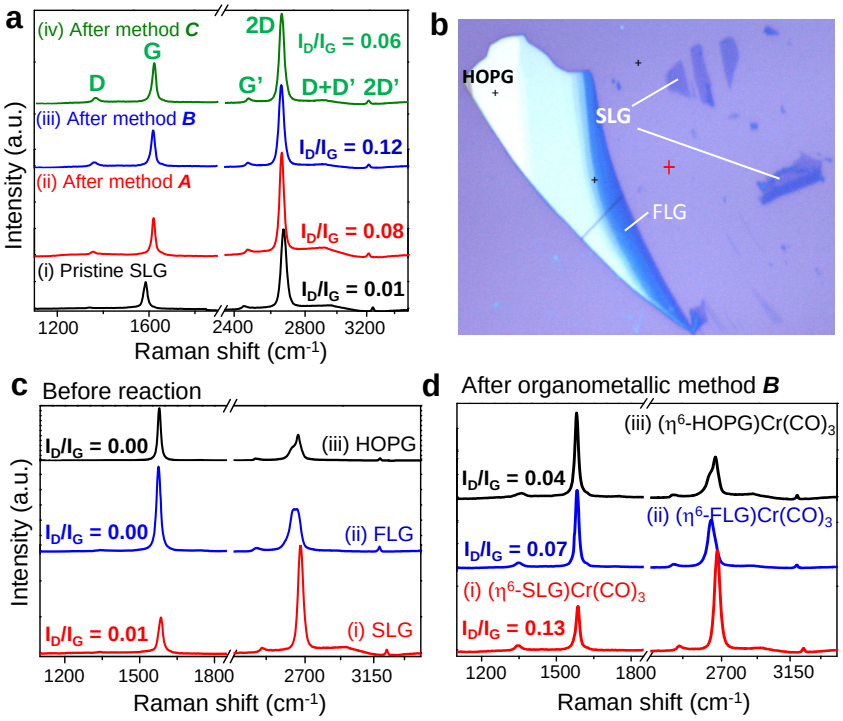

FIGURE 5.2. Organometallic functionalization of graphene and graphite. (a) Raman spectra of pristine SLG and Cr-functionalized graphene flakes, prepared by methods ***A***, ***B*** and ***C***. (b) Optical image of single-layer graphene (SLG), few layers graphene (FLG) and graphite (HOPG) on SiO_2/Si substrate. (c) Changes in chemical reactivity with stacking demonstrated by the evolution of Raman spectra before and after functionalization using method ***B*** on (i) SLG, (ii) FLG and (iii) HOPG.

5.2. Experiment Setup and Procedures

Materials and Instruments: Chromium(0) hexacarbonyl [98%, $Cr(CO)_6$, F.W.

= 220.06, m.p. = 150 C, b.p. = 210 ^{o}C (decomposes)], tris(acetonitrile)tricarbonylchromium(0) [$Cr(CO)_3(CH_3CN)_3$, F.W. = 259.18, m.p. = 67-72 ^{o}C (decomposes)], naphthalene (F.W. = 128.17, m.p.= 80.26 ^{o}C), *n*-dibutylether (b.p.= 140-142 ^{o}C), anhydrous tetrahydrofuran (b.p.= 66 ^{o}C), and anisole (b.p. = 154 ^{o}C) were all obtained from Sigma-Aldrich. All chromium reagents have high vapor pressures and direct exposure to the reagents should therefore be avoided. Raman spectra were collected in a Nicolet Almega XR Dispersive Raman microscope with a 0.7 μm spot size and 532 nm laser excitation. Scanning electron microscopy (SEM) images were acquired in a XL30-FEG SEM instrument. Electrospray ionization mass spectroscopy (ESI-MS) analysis was performed using the Agilent LCTOF instrument.

Device Farbication: Single-layer graphene flakes were isolated from bulk graphite by using standard micromechanical exfolaition technique and are placed on an oxidized silicon wafer (with 300 nm SiO_2). The contacts were deposited by standard e-beam lithography (Cr/Au – 10 nm/150 nm).

Organometallic Complexation Reactions: The hexahapto metal complexations reactions were perfomed at elevated temperatures under argon atmosphere using either chromium hexacarbonyls (in absence or presence of naphthalene as an additional ligand, method ***A*** and ***B*** respectively), or tris(acetonitrile)tricarbonylchromium (method ***C***).

Method A: SLG devices were immersed in a chromium hexacarbonyl [$Cr(CO)_6$, 0.1M] solution in dibutyl ether/tetrahydrofuran (THF) (5:1) and refluxed under argon atmosphere at 140 ^oC for 48 h. After functionalization the graphene devices were washed carefully with THF.

Method B: SLG devices were immersed in a solution of $Cr(CO)_6$ (as in method ***A***), with the addition of 0.25 equivalents of naphthalene ligand and heated to 80 ^oC for 12 hours.

Method C: SLG device was immersed in a solution of tris(acetonitrile) tricarbonylchromium(0) [$Cr(CO)_3(CH_3CN)_3$] in THF (~0.1 M) inside a glove-box and the reaction vessel was closed with rubber septum to maintain the argon atmosphere. The reaction vessel containing the graphene device and the solution were removed from the glove-box, connected to an argon line and heated slowly from room temperature to 40 ^oC for 6 hours. This procedure required rigorous exclusion of the atmosphere in order to avoid doping the graphene as a result of the decomposition of the chromium reagent to chromium oxide.

Decomplexation Reactions: In a typical reaction, the organometallic (η^6-SLG)$Cr(CO)_3$ complex was refluxed (150 ^oC) in presence of excess anisole (~10 mL) under an atmosphere of argon overnight. The resulting SLG flake was washed with chloroform, acetone, and hexane; dried with gentle flow of argon. The decomplexation product of (η^6-SLG)$Cr(CO)_3$ with anisole yielded a light

yellow solution, which was analyzed (after concentration with a rotary evaporator) using electrospray ionization mass spectroscopy (ESI-MS), which confirmed the chemical composition as (η^6-anisole)$Cr(CO)_3$ (chemical formula: $C_{10}H_8CrO_4$, F.W. = 243.98). ESI-MS data shows: m/z = 243.9832 [{(M+H)+[-H]}, diff(ppm): 3.88, $C_{10}H_8CrO_4$, calculated m/z = 243.9822], and m/z = 244.9904 $[(M+H)]^+$, diff(ppm): 1.36, $C_{10}H_9CrO_4$, calculated m/z = 244.9901].

Transport Measurements of the Devices: The devices were placed into a custom-built helium cryostat. All the measurements were performed in a high vacuum enviornment. The temperature of the devices was measured with a semiconductor thermometer mounted in close proximity to the chip carriers. Data were acquired by National Instrument PCI-6251 card controlled by a C++ based program.

5.3. Transport Features

In order to understand the effect of the hexahapto (η^6-) covalent binding of chromium (Cr) atoms on the electronic properties of graphene, transport measurements were performed before and after functionalization of the devices. Because the Cr-graphene product can decompose at elevated temperatures,[12,24] the (η^6-SLG)$Cr(CO)_3$ devices were characterized without annealing prior to the measurements. More than 10 devices were studied; in the present manuscript we

report results on two devices prepared with Method ***A*** and Method ***C***, respectively. Based on the Raman spectra (Figure 5.2a) and the transport measurements, the former device appears to have a higher degree of functionalization.

Figure 5.3a shows the zero-bias conductance (G) as a function of the applied gate voltage (V_g) of one pristine graphene device. The estimated room temperature field effect mobility of this device is μ~4000 cm^2/Vs.

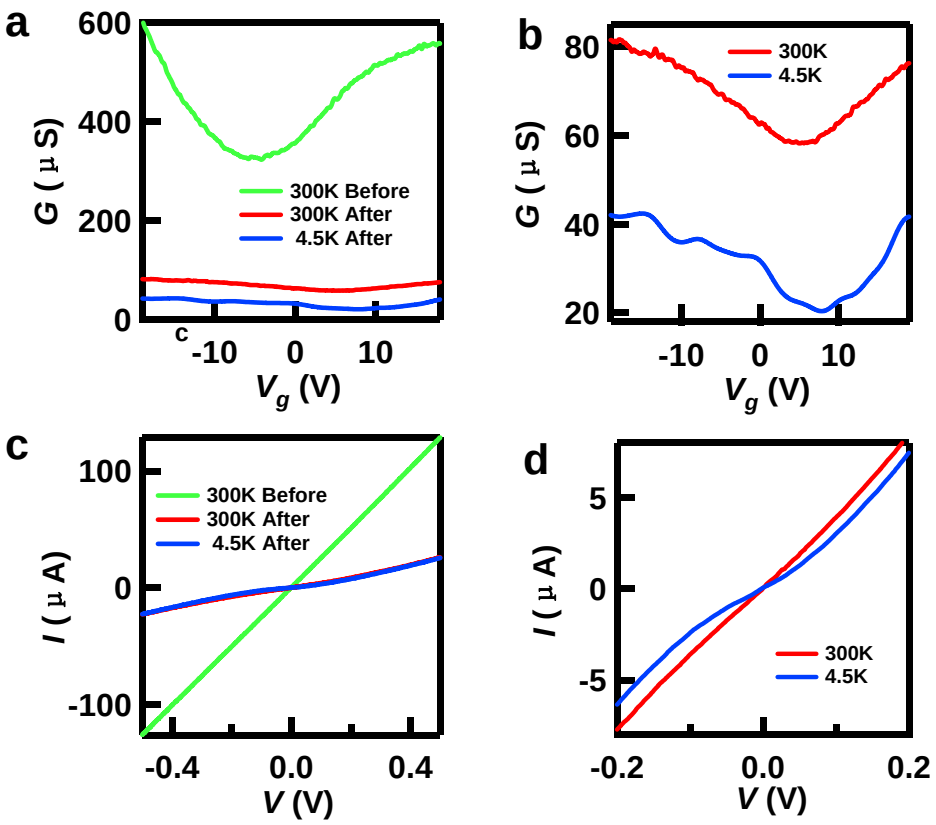

FIGURE 5.3. **(a)** $G(V_g)$ characteristic from a device before and after functionalization. **(b)** $G(V_g)$ characteristic of the functionalized device at 300K and 4.5K. **(c)** *I(V)* curves of the device before and after functionalization. **(d)** *I(V)* curves of the functionalized device at 300K and 4.5K.

The pristine graphene device shows linear current-voltage (*I-V)* characteristics up to 0.5 V (Figure 5.3c). Both the *I-V* and $G(V_g)$ curves of the pristine graphene device displayed weak temperature dependence, in agreement with previous experiments.[20] After functionalizing with chromium (method ***A***), the device's transport characteristics changed significantly: the conductance of the device decreased 10 times (Figure 5.3a, 5.3b) and the *I(V)* curves became non-linear in the temperature interval 4 K – 300 K, as shown in Figure 5.3c and 5.3d. The estimated field effect mobility of the functionalized device is μ~200 cm^2/Vs, which while significantly diminished, is higher than previously reported values for functionalized graphene.[3,20,34,35]

In order to explore the possibility of achieving high-mobility functionalized graphene devices, Cr-SLG devices derived by method ***C*** were characterized. Typically method ***C*** produced $(\eta^6\text{-SLG})Cr(CO)_3$ devices with room temperature field effect mobility in the range of ~2,000 cm^2/Vs and a current ON/OFF ratio of 5 to 13. The *G(V)* and *I(V)* curves at room temperature and 4.5 K of a weakly

functionalized device [(η^6-SGL)Cr(CO)$_3$ – method ***C***] are shown in Figure 5.4.

To understand the transport mechanism of the functionalized graphene device, the temperature dependences of conductance at the Dirac point and highly-doped regimes, were recorded in the range of 4 K to 300 K. The two most common transport mechanisms in functionalized devices are[20]: (1). thermal activation, in which conductance decreases exponentially with the ratio between the activation barrier Δ and thermal energy k_BT, $G \propto e^{-\Delta/2k_BT}$ (k_B - Boltzmann constant); (2). variable range hopping (VRH), which displays a stretched exponential dependence $G \propto e^{-(T_0/T)^{\alpha}}$, where T_0 is a characteristic temperature and α~ ½ to ¼ is the exponent. To analyze the data, we plot G on a logarithmic scale as a function of T^{-1} or $T^{-1/3}$ (see SI). In both plots, the data points do not fall on a straight line, suggesting that neither thermal activation nor VRH is the underlying transport mechanism in the functionalized devices. One possible complication is the variation in the mobility of the chromium atoms with temperature; such fluxional behavior has been observed in previous studies of polyaromatic hydrocarbon ligands,[36,37] and may be operative on the two-dimensional surface of the organometallic (η^6-SLG)Cr(CO)$_3$ complexes.[12]

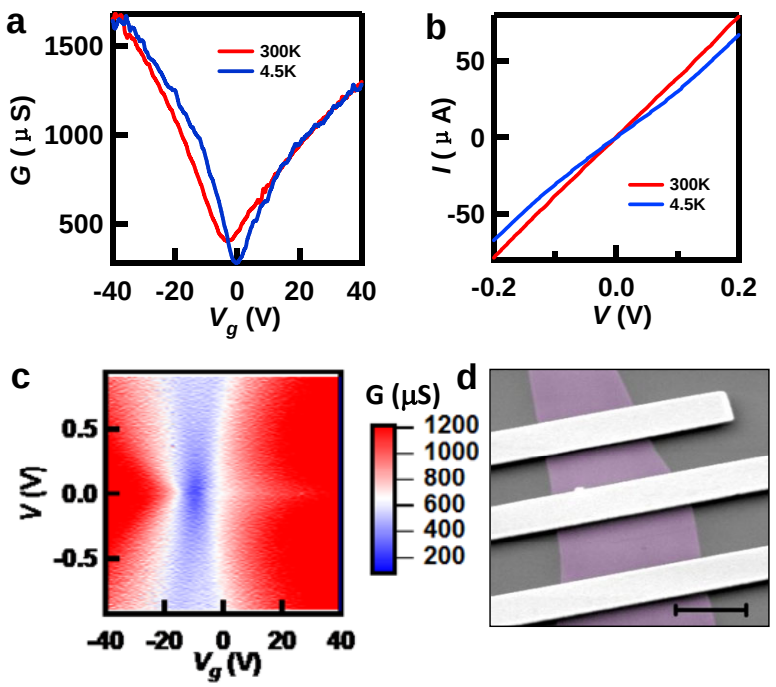

FIGURE 5.4. (a,b) *G(V)* characteristics and *I(V)* curves of a weakly functionalized device at 300 K and 4.5 K. The functionalized device has a mobility of ~2,000 cm^2/Vs at room temperature and ~3,500 cm^2/Vs at 4.5 K. (c) Conductance *G* as a function of bias *V* and gate V_g at 4.5 K of the same device. (d) SEM image of a typical device (scale bar 2 μm).

Another important characteristic of the chromium functionalization is its reversibility via decomplexation reactions. To achieve decomplexation the functionalized devices, $(\eta^6\text{-SLG})Cr(CO)_3$, were exposed to an electron-rich ligand, such as anisole (Figure 5.5a). In a typical reaction, the device with an organometallic $(\eta^6\text{-SLG})Cr(CO)_3$ complex was heated (150 ^oC) in presence of

excess anisole (~10 mL) under argon for 12 hours. The device was then washed with chloroform, acetone, and hexane and dried under argon.

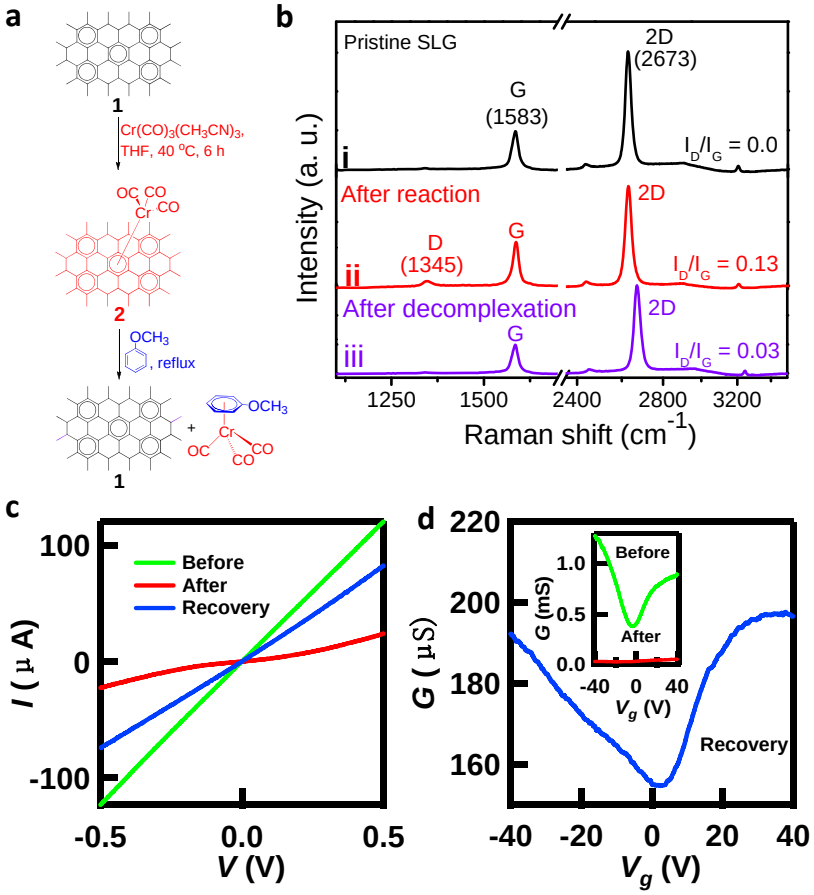

FIGURE 5.5. Decomplexation of chromium-graphene complexes. (a) Schematics of the complexation of the aromatic rings of graphene with $Cr(CO)_3$ moieties by use of $Cr(CH_3CN)_3(CO)_3$ reagents (method ***C***), and decomplexation of the same using electron-rich ligand – anisole, to regenerate a clean graphene and (η^6-anisole)$Cr(CO)_3$. (b) Raman spectra of single layer graphene (SLG) – *i*: before reaction, *ii*: after reactions with tris(acetonitrile)tricarbonylchromium

$[Cr(CO)_3(CH_3CN)_3]$, and *iii*: after decomplexation. (c) *I(V)* curves and (d) *G* (V_g) curves of SLG device: green - pristine device, red – Cr-functionalized graphene device, blue – functionalized device after chemical recovery with anisole ligands. The measurements were performed at room temperature.

The complexation and decomplexation reactions were followed by Raman spectroscopy. As shown in Figure 5.5b, the intensity of the D-band was significantly reduced after the decomplexation reaction ($I_D/I_G = 0.03$). Mass spectroscopic (ESI-MS) analysis of the concentrated extract, which resulted from the competitive arene exchange reaction between (η^6-SLG)$Cr(CO)_3$ and anisole, led to the identification of a product corresponding to (η^6-anisole)$Cr(CO)_3$, which was detected with m/z = 243.9832. The transport measurements showed that the conductance and mobility of the devices were increased, although a complete recovery of the pristine device performance was not observed.

To further investigate the properties of our devices, we compare the temperature dependence of pristine and functionalized devices. Typically, the conductance of pristine single-layer graphene devices has very weak temperature dependence, as shown in Figure 5.6 In contrast, a moderate temperature dependence of conductance is observed for the chromium functionalized single-layer graphene devices. The zero bias conductance of a Cr functionalized graphene device as a function of temperature in different doping regimes is

illustrated in Figure 5.7. The conductance data is plotted as a function of T^{-1} and $T^{-1/3}$. The results thus suggest that transport through functionalized devices is via variable range hopping.

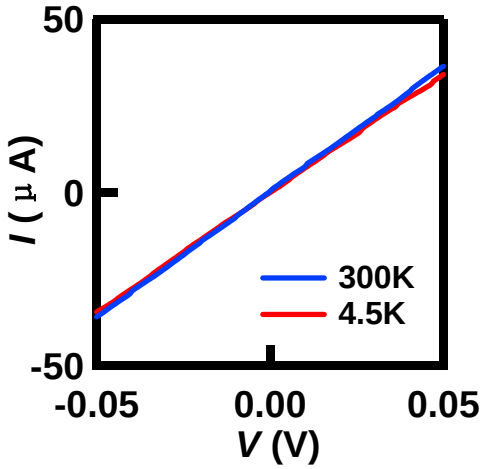

FIGURE 5.6. I-V curves at Dirac point of a pristine graphene device at T = 300 K and 4.5 K.

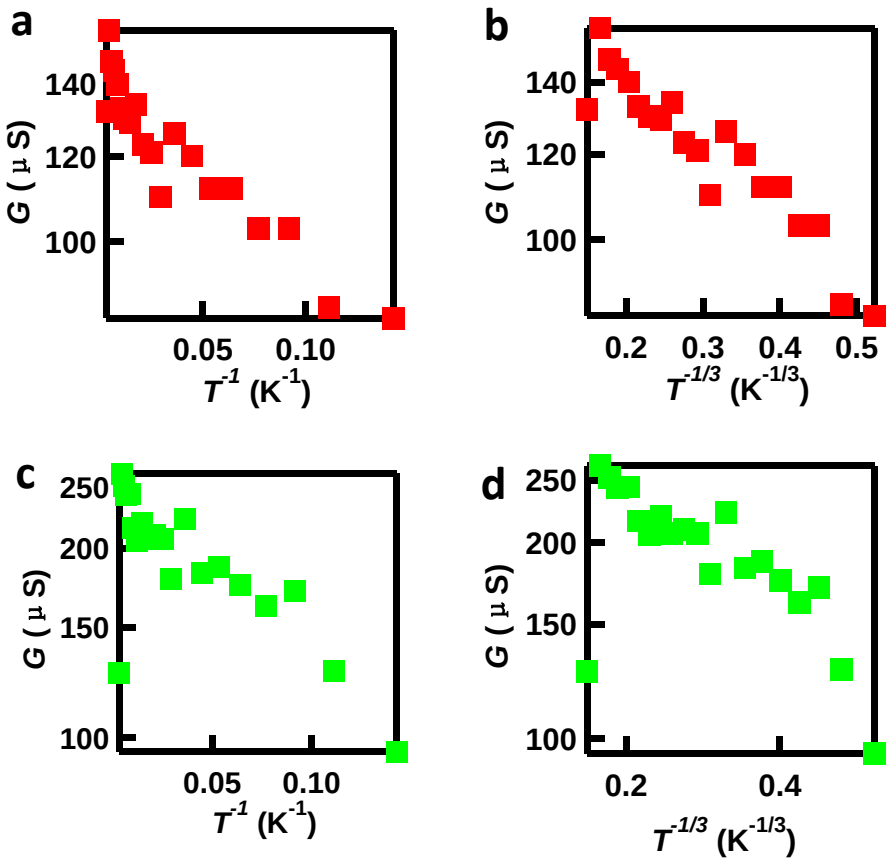

FIGURE 5.7. (a,b) Zero bias conductance, G at the Dirac point vs T^{-1} and $T^{-1/3}$ for a chromium (Cr) fuctionalized graphene device. (c, d) Zero bias conductance G at a highly doped regime (Dirac point – 62V) vs T^{-1} and $T^{-1/3}$.

5.4. Conclusion

In summary, we find that the mono-hexahapto-chromium complexation of single layer graphene allows the fabrication of high performance chemically functionalized devices. We demonstrated that chemically modified graphene devices with a room-temperature field effect mobility in the range of μ ~200 -

2,000 cm^2/Vs and an on/off ratio of 5 to 13 can be fabricated via η^6-metal complexation of graphene. Furthermore the graphene organometallic complexation chemistry may be reversed by treatment of the devices with electron rich ligands. These graphene-metal complexes are potential candidates for advanced molecular wires,[38] spintronic devices,[39] and organometallic catalyst supports[12,40]. The finding that the in-plane transport properties are retained in the presence of mono-hexahapto-coordinated transition metals encourages the pursuit of this mode of bonding in 2-D and 3-D structures, which employ bis-hexahapto-metal complexation.[12,23-26]

References:

1 J. H. Chen, C. Jang, S. D. Xiao, M. Ishigami, M. S. Fuhrer, *Nature Nanotech.* **2008**, *3*, 206.

2 S. Ryu, M. Y. Han, J. Maultzsch, T. F. Heinz, P. Kim, M. Steigerwald, L. E. Brus, *Nano Lett.* **2008**, *8*, 4597.

3 D. C. Elias, R. R. Nair, T. M. G. Mohiuddin, S. V. B. Morozov, P., M. P. Halsall, A. C. Ferrari, D. W. Boukhvalov, M. I. Katsnelson, A. K. Geim, K. S. Novoselov, *Science* **2009**, *323*, 610.

4 S. B. Bon, L. Valentini, R. Verdejo, J. L. G. Fierro, L. Peponi, M. A. Lopez-Manchado, J. M. Kenny, *Chem. Mater.* **2009**, *21*, 3433.

5 F. Withers, M. Dubois, A. K. Savchenko, *Phys. Rev. B* **2010**, *82*, 073403.

6 E. Bekyarova, M. E. Itkis, P. Ramesh, C. Berger, M. Sprinkle, W. A. de Heer, R. C. Haddon, *J. Am. Chem. Soc.* **2009**, *131*, 1336.

7 E. Bekyarova, M. E. Itkis, P. Ramesh, R. C. Haddon, *Phys. Stat. Sol. RRL* **2009**, *3*, 184.

8 K. P. Loh, Q. L. Bao, P. K. Ang, J. X. Yang, *J. Mater. Chem.* **2010**, *20*, 2277.

9 R. Sharma, J. H. Baik, C. J. Perera, M. S. Strano, *Nano Lett.* **2010**, *10*, 398.

10 A. Sinitskii, A. Dimiev, D. A. Corley, A. A. Fursina, D. V. Kosynkin, J. M. Tour, *ACS Nano* **2010**, *4*, 1949.

11 S. Sarkar, E. Bekyarova, S. Niyogi, R. C. Haddon, *J. Am. Chem. Soc.* **2011**,

133, 3324.

12 S. Sarkar, S. Niyogi, E. Bekyarova, R. C. Haddon, *Chem. Sci.* **2011**, *2*, 1326.

13 S. Niyogi, E. Bekyarova, M. E. Itkis, H. Zhang, K. Shepperd, J. Hick, M. Sprinkle, C. Berger, C. N. Lau, W. A. de Heer, E. H. Conrad, R. C. Haddon, *Nano. Lett.* **2010**, *10*, 4061–4066.

14 N. Jung, N. Kim, S. Jockusch, N. J. Turro, P. Kim, L. Brus, *Nano Lett.* **2009**, *9*, 4133.

15 S. Sarkar, E. Bekyarova, R. C. Haddon, *Acc. Chem. Res.* **2012**, *45*, 673.

16 S. Sarkar, E. Bekyarova, R. C. Haddon, *Angew. Chem. Int. Ed.* **2012**, *51*, 4901; *Angew. Chem.* **2012**, *124*, 4985.

17 S. Niyogi, E. Bekyarova, J. Hong, S. Khizroev, C. Berger, W. A. de Heer, R. C. Haddon, *J. Phys. Chem. Lett.* **2011**, *2*, 2487.

18 E. Bekyarova, S. Sarkar, S. Niyogi, M. E. Itkis, R. C. Haddon, *J. Phys. D: Appl. Phys.* **2012**, *45*, 154009.

19 J. Hong, S. Niyogi, E. Bekyarova, M. E. Itkis, R. Palanisamy, N. Amos, D. Litvinov, C. Berger, W. A. de Heer, S. Khizroev, R. C. Haddon, *Small* **2011**, *7*, 1175.

20 H. Zhang, E. Bekyarova, J.-W. Huang, Z. Zhao, W. Bao, F. Wang, R. C. Haddon, C. N. Lau, *Nano Lett.* **2011**, *11*, 4047.

21 S. Sarkar, E. Bekyarova, R. C. Haddon, *Mater. Today* **2012**, *15*, 276.

22 T. O. Wehling, S. Yuan, A. I. Lichtenstein, A. K. Geim, M. I. Katsnelson, *Phys. Rev. Lett.* **2010**, *105*, 056802.

23 F. Wang, M. E. Itkis, E. Bekyarova, X. Tian, S. Sarkar, A. Pekker, I. Kalinina, M. Moser, R. C. Haddon, *Appl. Phys. Lett.* **2012**, *100*, 223111.

24 I. Kalinina, E. Bekyarova, S. Sarkar, F. Wang, M. E. Itkis, X. Tian, S. Niyogi, N. Jha, R. C. Haddon, *Macromol. Chem. Phys.* **2012**, *213*, 1001.

25 F. Wang, M. E. Itkis, E. Bekyarova, S. Sarkar, X. Tian, R. C. Haddon, *J. Phys. Org. Chem.* **2012**, *25*, 607.

26 X. Tian, S. Sarkar, M. L. Moser, F. Wang, A. Pekker, E. Bekyarova, M. E. Itkis, R. C. Haddon, *Mater. Lett.* **2012**, *80*, 171.

27 J. Moser, A. Barreiro, A. Bachtold, *Appl. Phys. Lett.* **2007**, *91*, 163513.

28 E. P. Kundig, C. Perret, S. Spichiger, G. Bernardinelli, *J. Organomet. Chem.* **1985**, *286*, 183.

29 Y. Kondo, J. R. Green, J. W. Ho, *J. Org. Chem.* **1993**, *58*, 6182.

30 E. P. Kundig, *Topics Organomet. Chem.* **2004**, *7*, 3.

31 G. A. Moser, M. D. Rausch, *Syn. Reactiv. Inorg. Metal-Org. Chem.* **1974**, *4*, 37.

32 J. Vebrel, R. Mercier, J. Belleney, *J. Orgmet. Chem.* **1982**, *235*, 197.

33 J. A. Morley, N. F. Woolsey, *J. Org. Chem.* **1992**, *57*, 6487.

34 J. T. Robinson, J. S. Burgess, C. E. Junkermeier, S. C. Badescu, T. L.

Reinecke, F. K. Perkins, M. K. Zalalutdniov, J. W. Baldwin, J. C. Culbertson, P. E. Sheehan, E. S. Snow, *Nano Lett.* **2010**, *10*, 3001.

35 R. R. Nair, W. Ren, R. Jalil, I. Riaz, V. G. Kravets, L. Britnell, P. Blake, F. Schedin, A. S. Mayorov, S. Yuan, M. I. Katsnelson, H. M. Cheng, W. Strupinski, L. G. Bulusheva, A. V. Okotrub, I. V. Grigorieva, A. N. Grigorenko, K. S. Novoselov, A. K. Geim, *Small* **2010**, *6*, 2877.

36 J. O. C. Jimenez-Halla, J. Robles, M. Sola, *Organometallics* **2008**, *27*, 5230.

37 A. S. Filatov, M. A. Petrukhina, *Coord. Chem. Rev.* **2010**, *254*, 2234.

38 J. Jiang, J. R. Smith, Y. Luo, H. Grennberg, H. Ottosson, *J. Phys. Chem. C* **2011**, *115*, 785.

39 S. M. Avdoshenko, I. N. Ioffe, G. Cuniberti, L. Dunsch, A. A. Popov, *ACS Nano* **2011**, *5*, 9939.

40 R. D. Adams, B. Qu, *Organometallics* **2000**, *19*, 2411.

Chapter 6

Suspended graphene based switch

In this chapter, we focus on switching behavior in suspended few layer graphene devices that are “broken” using a pulsed electrical breakdown technique. The conductance of the resulting devices can be programmed by the application of voltage pulses, with a voltage of 2.5V~4.5V corresponding to an ON pulse and voltages ~8V corresponding to OFF pulses. Electron microscope imaging of the devices shows that the graphene sheets typically remain suspended and that the device conductance tends to zero when the observed gap is large. The switching rate is strongly temperature dependent, which rules out a purely electromechanical switching mechanism. This observed switching in suspended graphene devices strongly suggests a switching mechanism via atomic movement and/or chemical rearrangement, and underscores the potential of all-carbon devices for integration with graphene electronics.

We will start this chapter by introducing electronic break down carbon systems (carbon nano-tubes and graphene/graphite flakes) and behaviors of our

devices in working state. In Section 6.2 we will describe the detailed fabrication and electronic breakdown process of suspended graphene devices. In Section 6.3 we will discuss the measurement process, performance of our devices and *in situ* observation via SEM (scanning electron microscope) imaging. Based upon those data and observations, we proposed mechanisms behind switching behavior.

6.1 Electronic Breakdown in Carbon System

Long-term archival information storage is an open challenge with a variety of approaches proposed, [1] including periodic migration to new media. However, such approaches require constant effort to avoid loss due to data errors caused by finite storage medium lifetime. A nonvolatile means of storing information densely which is stable for extended time periods is therefore highly desirable. One approach to address this issue is to store information in the arrangement of atoms rather than electrical charges. Previous work has shown the electromigration of metallic particles in multiwalled carbon nanotubes (MWNTs).[2,3] More recently, conductance switching was observed in graphene and graphitic break junctions, and the proposed switching mechanism was the formation and breakdown of carbon chains or filaments.[4,5] However, later works reported cyclable conductance switching in devices solely consists of electrodes on SiO2 interrupted by nanogaps,[6,7] thus it remains controversial whether the swiching behavior in

substrate-supported devices is intrinsic or merely arising from the underlying substrate.

To determine the role of the substrate in producing the switching behavior and to gain more insight into electromigration and switching in graphene, we study switching in suspended graphene layers that are isolated from the substrate.[8–10] We demonstrate that switching in such suspended graphene break junctions has similar behavior to that of substrate-supported devices. The switches are formed by a breakdown of graphene which leaves a small gap, using a sequential breakdown technique. The junction resistance can be controlled by the application of voltage pulses, with 4 V corresponding to an ON pulse that decreases the device resistance and 8 V corresponding to an OFF pulse that increases the device resistance. The devices can be cycled up to hundreds of times before becoming inoperative. Scanning electron microscopy (SEM) imaging of the gap in the ON and OFF states shows a larger gap in the OFF state than the ON state. The similarity of the switching characteristics in suspended devices strongly suggests that the switching mechanism is the same as on substrate supported samples (though oxide breakdown cannot be unequivocally excluded). The switching rate depends strongly on temperature, which indicates that atomic motion, chemical rearrangement, or both are essential to the switching mechanism.

6.2 Device Fabrication and Breakdown Process

Few-layer graphene sheets (typically 1−5 layers thick) are mechanically exfoliated over Si substrates covered by a layer of 300 nm thick SiO_2 and identified by optical microscopy.[11] The switch devices are fabricated with two different methods: (i) Using electron beam lithography (EBL) to fabricate the device on a graphene sample on the SiO_2/Si substrate and then etching ~120 nm SiO_2 under the graphene flakes by dipping the device into a buffered oxide etch solution;[9,10] and (ii) graphene is exfoliated onto substrates that are prepatterned with trenches, which are 250 nm deep and 2.5−5 μm wide. Source and drain electrodes that consist of 10 nm of Ti and 70 nm of Au are deposited by evaporation through a shadow mask, [12] which is aligned carefully with the edge of the trenches. This approach minimizes the risk of sample collapse during the conventional EBL procedure. A completed device is shown in the inset to Figure 6.1a, while the main panel plots the current I and the voltage V applied to the device versus time. I is approximately linear in V up to ~0.5 V, with a two-terminal conductance $G \sim 0.5$ mS.

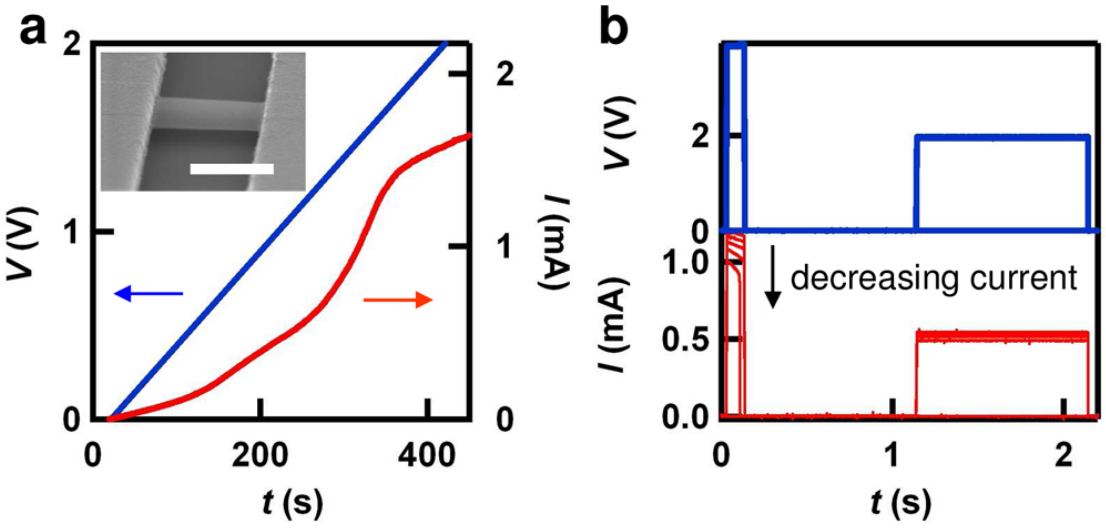

FIGURE 6.1. (a) The *IV−time* curve of a suspended graphene device. The blue curve indicates the bias voltage, and the red curve indicates the corresponding current. The inset shows the SEM image of the device. The scale bar is 1 μm. (b, upper panel) The voltage sequence which is used to break down suspended sample. The pulse voltage is 3.9 V, the test voltage after the pulse is 1.95 V. (b, lower panel) The current response of the device during breakdown. After the last pulse, the sample is completely broken, and under the test voltage (1.95 V), the corresponding current is zero.

To create the switch, we perform the breakdown step using a modification of the electromigration technique that was reported previously.[4]The completed device is placed in a high vacuum, typically $\sim 10^{-6}$ Torr, and voltage pulses ($\sim$4 V, typical duration 0.1 s) are applied. These pulses sequentially reduce the device

conductance until it becomes zero (Figure 6.1b). The advantage of "pulse-breakdown" technique is protecting the suspended graphene flakes from failing down to the substrate at the right moment when they are breaking down. Since a constant or a constant increasing voltage can drag the suspended halves of graphene flakes down to the bottom after cracks extending across the whole flakes. (This condition can be observed in our Supporting Information: http://pubs.acs.org/doi/suppl/10.1021/nl203160x) The typical breaking current density is ~2 mA/μm. Figure 6.2a−c shows the breakdown of another device. The device began its breakdown near the geometric center, and the broken region expanded upon further application of voltage until the breakdown was complete (Figure 6.2c). An *in situ* SEM video of the breakdown process is available as Supporting Information. While breakdown often began at the center, for some samples, the breakdown began at the edge but was still centrally located relative to the electrodes. This suggests that the device temperature plays a critical role in the breakdown, [13, 14] though it is not the only factor. Other factors, such as fluctuations and defects, are also likely to be important parameters during electromigration.

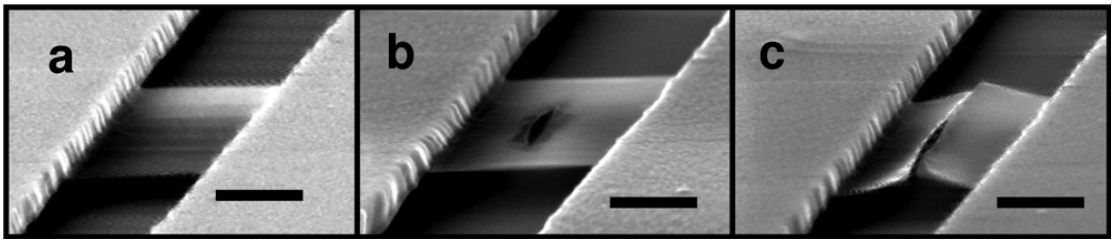

FIGURE 6.2. (a) A suspended sample before breakdown and (b) the broken region started from the center and expanded. The image was taken after a 3 V pulse was applied. (c) After increasing the amplitude of the pulse voltage, the sample was completely broken but still freestanding. The image was taken after an 8 V pulse was applied. The scale bar indicates 500 nm.

6.3 Measurement and Mechanisms

Figure 6.3a shows the *IV* characteristic of a device following a successful breakdown. When the voltage is swept from −8 to +8 V, at first the current is zero. When the voltage is ~4 V, the current rises, often by a series of step-like current jumps, indicating that the device is entering the "ON" state. As the voltage is raised further, the device conductance decreases to zero, turning the device "OFF." The sweep in the reverse direction from +8 to −8 V shows similar behavior. We note that the high vacuum is crucial for producing an operable switch device, presumably because of the removal of molecules that may contaminate or react with graphene devices, such as oxygen or water vapor. To

exclude the possibility that the substrate contributes to the measured current by a parallel conduction path, we made a control device with the same exact fabrication procedure, including electrodes that are partially released from the substrates via etching, but without the graphene. These devices showed little or no measurable current up to the maximum voltage (10 V) used in our experiments (Figure 6.3b). Breakdown did occur, however, at significantly higher voltages ～210 V. This demonstrates the presence of the graphene layer is essential for obtaining a measurable current within the 10 V voltage range employed in the experiment.

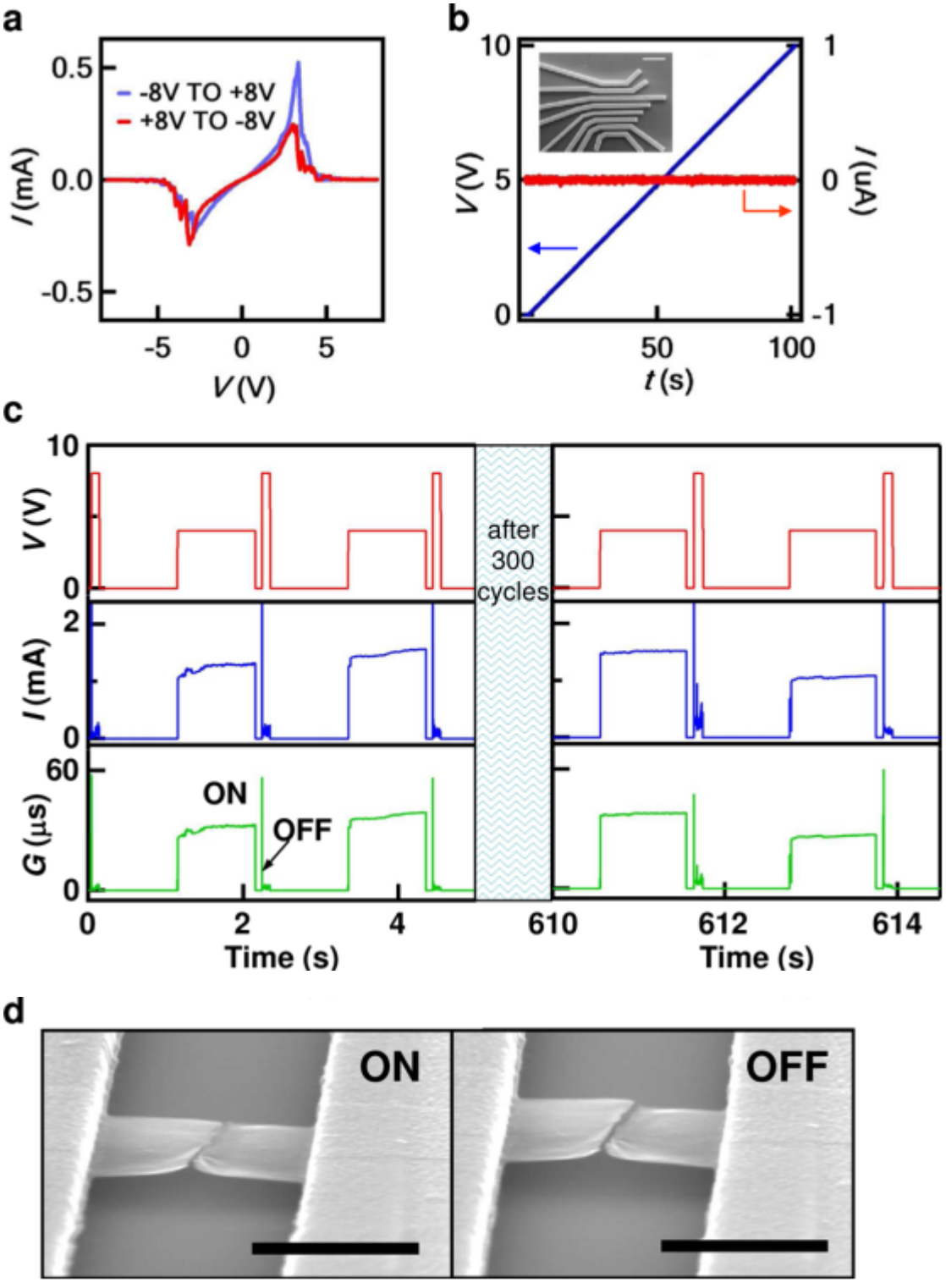
a
0.5
0.0
-0.5
-8V TO +8V
+8V TO -8V
I (mA)
-5
0
5
V (V)
b
10
5
0
1
0
-1
V (V)
I (uA)
50
100
t (s)
c
10
0
V (V)
2
0
I (mA)
60
0
G (μs)
ON
OFF
after
300
cycles
0
2
4
610
612
614
Time (s)
Time (s)
d
ON
OFF

FIGURE 6.3. (a) The *IV* curve after breakdown. The voltage ramp from −8 to +8 V is shown as the blue curve, and the voltage ramp back from +8 V to −8 V is shown as the red curve. (b) The *IV*−*time* curve of a pure SiO_2 device, which has the same geometry and etching procedure as the device shown in Figure 6.1a, without the presence of graphene. The blue curve indicates the voltage, and the red curve indicates the current. The current is approximately zero for voltage up to 10 V. The inset shows the SEM image of the control device. The scale bar is 10 μm. (c) The repeatability of the switching behavior. From top to bottom, the panels display the applied voltage *V*, the current response I, and the device conductance $G = I/V$ as a function of time *t*, respectively. Left panel: initial behavior. Right panel: after 300 switching cycles. (d) The SEM images of ON and OFF state for a different device. The scale bar is 1 μm.

The switching behavior in the suspended devices was reproducible, and the most stable devices could be switched many times. The switching behavior is shown in Figure 6.3c. Applying an ON pulse of 4 V switches the device "ON", with typical conductance $G \sim 25-40$ μS; an OFF pulse of 8 V, on the other hand, reduces the conductance to ~1 μS. This behavior in suspended devices is very similar to that from single-layer graphene devices that are supported on the SiO_2 substrates.[4] This strongly suggests that the switching mechanisms are the same in

both cases and that switching occurs in an all-carbon device. Notably, these switches are nonvolatile and robust. For suspended devices, they can be switched up to hundreds of cycles. As a demonstration, the device behavior after 300 cycles is shown in the right panels of Figure 6.3c, which is very similar to that of the first two cycles. However it was found that the number of switching cycles before the device failure was less than that of those on substrates, as one may expect for the greater degree of fragility of suspended devices.

To understand better how the switching behavior occurred, we also imaged a different device by SEM in both the ON and OFF states (Figure 6.3d). We note that imaging the device during the switching cycles results in device degradation and failure, which is likely due to accumulation of amorphous carbon and destabilization by the electron beam.[15−17] In the OFF state, a gap is clearly visible in the image, while in the ON state, the gap appears considerably smaller. This provides another indication that the current flow in the device is strictly through the graphene sheet. Since the devices are suspended and can move freely, also suggesting the possibility that there is a nanomechanical component to the switching behavior.[18−21] For example, due to slack in the graphene sheet, the two halves of the original sheet that are present after the breaking procedure may be electrostatically attracted to each other when the source drain voltage is applied, completing the circuit when they come into contact. This step is expected to be

relatively fast. We estimate the characteristic frequency of a graphene cantilever with the typical geometry of our devices to be ~1 MHz. This sets an upper bound for initial switch closure of ~1μs. In this situation it is possible that there is some "switch bounce", where the layers rebound from each other after their initial contact. This motion would be damped by the intrinsic quality factor of the graphene layers, and with a typical quality factor~300 at room temperature,[22] the motion would be reduced to the atomic scale in t ~ 1 ms. Note that this estimate neglects dissipation by the collisions themselves[23] and is therefore an upper bound, likely an extreme one.

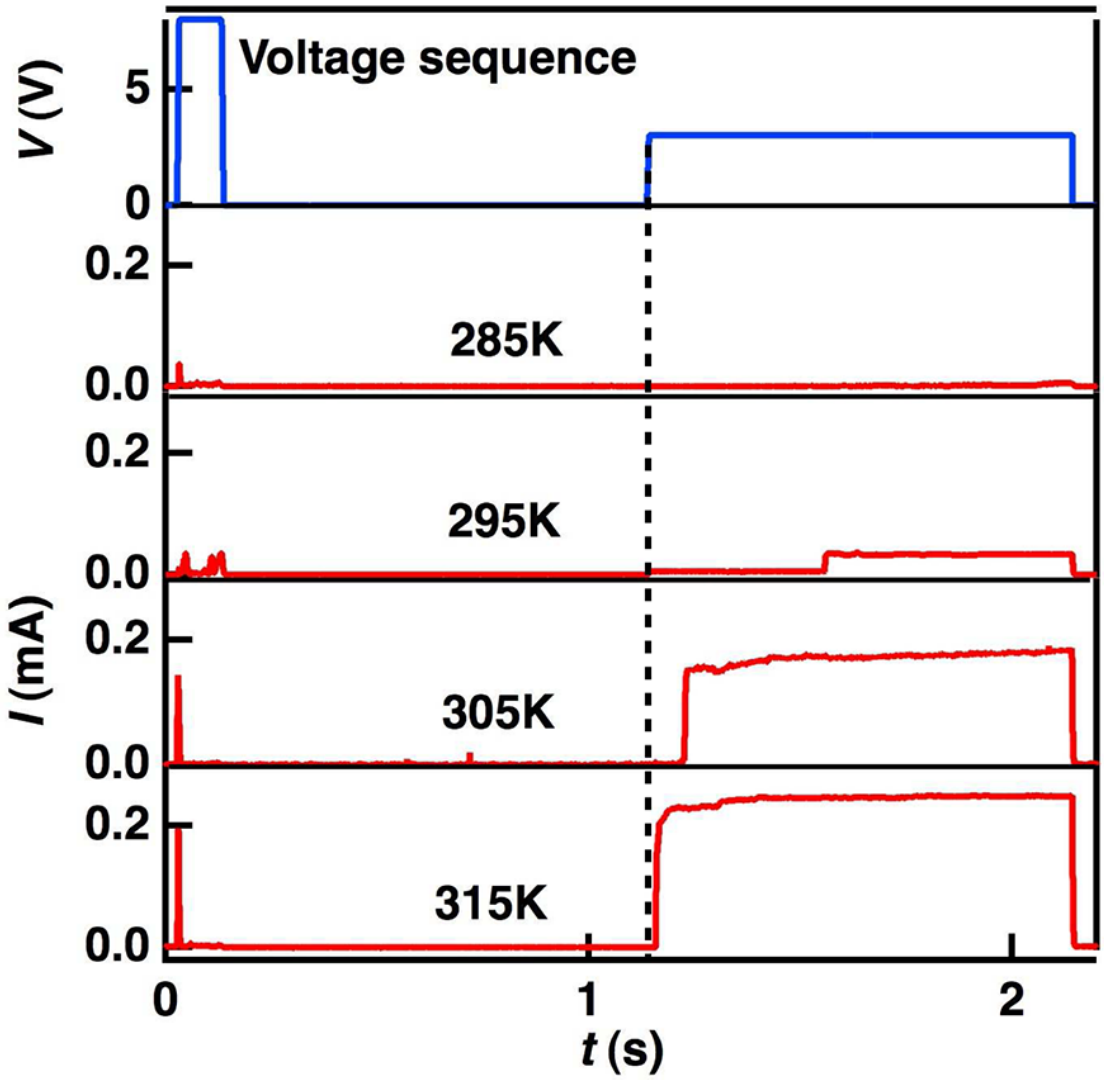

FIGURE 6.4. Typical current response versus time in a single switching cycle at different temperatures.

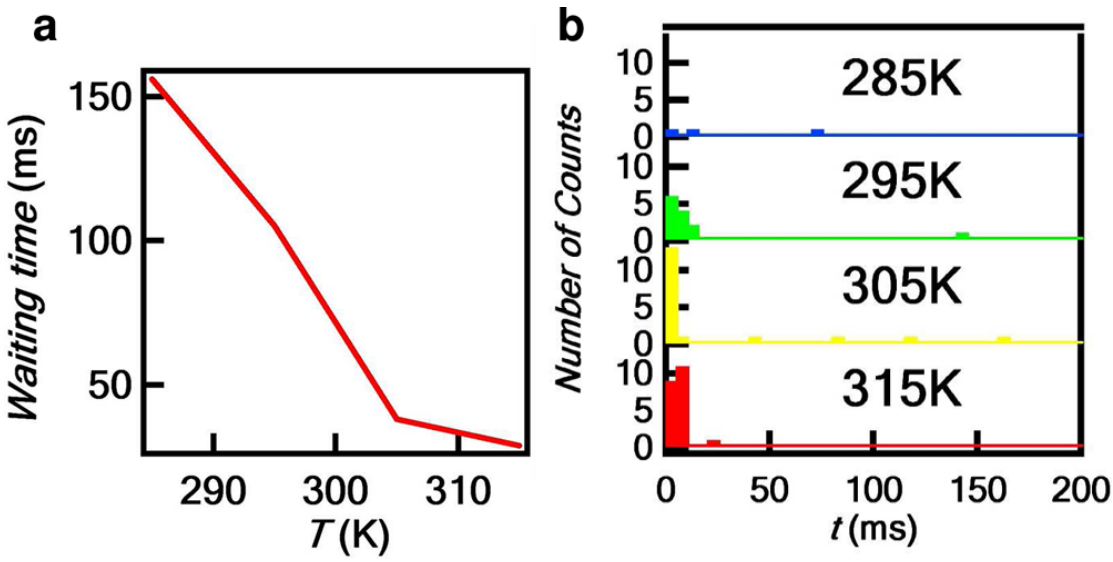

FIGURE 6.5. (a) Average waiting time vs temperature. (b) Statistical analysis of the waiting time.

To further investigate the switching mechanism, we studied the temperature dependence of the switching rate. Figure 6.4 shows the time lapse to switch into the ON state when a square pulse of height 3.0 V is applied, using curves with a switching time approximately equal to the average time measured for events within 1 s at each temperature, plotted versus temperature in Figure 6.5a. The switching rates are highly temperature sensitive and show a rapid increase as the temperature is raised. A histogram of the measured switching time for a range of temperatures is plotted in Figure 6.5b. As the temperature is lowered, longer intervals to switch become more common and very short intervals less common. The switching rates were also measured at lower temperatures; no switching was

observed at 4.5 K and indeed becomes very rare even below temperatures as large as 280 K. The long time scale for switching under appropriate conditions of >1 s greatly exceeds the upper bound estimate above t = 1ms. In addition, the rate of nanomechanical switching would be expected to have little temperature dependence over the temperature range studied based on the relatively constant elastic properties of the graphene sheets. This strongly indicates that the switching rate is not limited by nanomechanical motion but rather by a step that involves the motion of atoms and/or the rearrangement of chemical bonds that must overcome a barrier, which is on the order of ～eV, for example, by the formation of carbon chains.[4, 24, 25] Such atomic rearrangement, if elucidated in detail, may provide the basis for long-term storage. Estimates of the ultimate lifetime will require detailed understanding of the atomic motion that underlies the switching behavior. Such understating will require new experiments, such as STM studies, or observation of the switching using a transmission electron microscope.

References:

1 Baker, M.; Shah, M.; Rosenthal, D. S. H.; Roussopoulos, M. Maniatis, P.; Giuli, T.; Bungale, P. In Proceedings of the 1st ACM SIGOPS/EuroSys European Conference on Computer Systems 2006, Leuven, Belgium, April 18−21, 2006; Berbers, Y., Zwaenepoel, W., Eds.; ACM: New York, 2006, p 221.

2 Begtrup, G. E.; Gannett, W.; Yuzvinsky, T. D.; Crespi, V. H.; Zettl, A. *Nano Lett.* **2009**, *9*, 1835.

3 Svensson, K.; Olin, H.; Olsson, E. Phys. Rev. Lett. 2004, 93, 145901.

4 Standley, B.; Bao, W. Z.; Zhang, H.; Bruck, J.; Lau, C. N.; Bockrath, M. Nano Lett. 2008, 8, 3345.

5 Li, Y.; Sinitskii, A.; Tour, J. M. Nat. Mater. 2008, 7, 966.

6 Yao, J.; Zhong, L.; Zhang, Z.; He, T.; Jin, Z.; Wheeler, P. J.; Natelson, D.; Tour J. M. Small 2009, 5, 2910.

7 Yao, J.; Sun, Z.; Zhong, L.; Natelson, D.; Tour, J. M. Nano Lett. 2010, 10, 4105.

8 Bao, W. Z.; Miao, F.; Chen, Z.; Zhang, H.; Jang, W. Y.; Dames, C.; Lau, C. N. *Nat. Nanotechnol.* **2009**, *4*, 562.

9 Bolotin, K. I.; Sikes, K. J.; Jiang, Z.; Klima, M.; Fudenberg, G.; Hone, J.;

Kim, P.; Stormer, H. L. *Solid State Commun.* **2008**, *146*, 351.

10 Du, X.; Skachko, I.; Barker, A.; Andrei, E. Y. *Nat. Nanotechnol.* **2008**, *3*, 491.

11 Novoselov, K. S.; Geim, A. K.; Morozov, S. V.; Jiang, D.; Zhang, Y.; Dubonos, S. V.; Grigorieva, I. V.; Firsov, A. A. *Science* **2004**, *306*, 666.

12 Bao, W.; Liu, G.; Zhao, Z.; Zhang, H.; Yan, D.; Deshpande, A.; LeRoy, B.; Lau, C. *Nano Res.* **2010**, *3*, 98.

13 Collins, P. G.; Hersam, M.; Arnold, M.; Martel, R.; Avouris, P. *Phys. Rev. Lett.* **2001**, *86*, 3128.

14 Chiu, H. Y.; Deshpande, V. V.; Postma, H. W. C.; Lau, C. N.; Mikó, C.; Forró, L.; Bockrath, M. *Phys. Rev. Lett.* **2005**, *95*, 226101.

15 Childres, I.; Jauregui, L. A.; Foxe, M.; Tian, J. F.; Jalilian, R.; Jovanovic, I.; Chen, Y. P. *Appl. Phys. Lett.* **2010**, 97.

16 Xu, M.; Fujita, D.; Hanagata, N. *Nanotechnology* **2010**, *21*, 265705.

17 Teweldebrhan, D.; Balandin, A. A. *Appl. Phys. Lett.* **2009**, 94.

18 Rueckes, T.; Kim, K.; Joselevich, E.; Tseng, G. Y.; Cheung, C. L.; Lieber, C. M. *Science* **2000**, *289*, 94.

19 Kinaret, J. M.; Nord, T.; Viefers, S. *Appl. Phys. Lett.* **2003**, *82*, 1287.

20 Lee, S. W.; Lee, D. S.; Morjan, R. E.; Jhang, S. H.; Sveningsson, M.; Nerushev, O. A.; Park, Y. W.; Campbell, E. E. B. *Nano Lett.* **2004**, *4*, 2027.

21 Deshpande, V. V.; Chiu, H. Y.; Postma, H. W. C.; Mikó, C.; Forró, L.; Bockrath, M. *Nano Lett.* **2006**, *6*, 1092.

22 Bunch, J. S.; van der Zande, A. M.; Verbridge, S. S.; Frank, I. W.; Tanenbaum, D. M.; Parpia, J. M.; Craighead, H. G.; McEuen, P. L. *Science* **2007**, *315*, 490.

23 Jonsson, L. M.; Nord, T.; Kinaret, J. M.; Viefers, S. *J. Appl. Phys.* **2004**, *96*, 629.

24 Jin, C.; Lan, H.; Peng, L.; Suenaga, K.; Iijima, S. *Phys. Rev. Lett.* **2009**, *102*, 205501.

25. Rinzler, A. G.; Hafner, J. H.; Nikolaev, P.; Lou, L.; Kim, S. G.; Tomanek, D.; Nordlander, P.; Colbert, D. T.; Smalley, R. E. *Science* **1995**, *269*, 1550.

Chapter 7

Transport in Suspended graphene under strain

Graphene is a two dimensional carbon allotrope. Since its first isolation onto insulating substrates[1] and the subsequent development of wafer scale synthesis technology[2], graphene has attracted wide attention as a promising candidate for next generation nano-electronics[3-6]. Since it is also nature's thinnest membrane, inducing strain is an effective approach to modify the transports properties or band structure of pristine graphene[7-10]. Despite some progress in this area using optical methods[11,12], transport studies with *in situ* strain and the development of research platforms is still an opening field.

In this chapter, I will describe transport measurements of suspended graphene samples under *in situ* strain manipulation. These free-standing samples have free standing electrodes whose height can be controlled by adjusting back gate voltage, thus inducing strain in the suspended membranes. *In situ* SEM imaging shows successive stretching and relaxing of the graphene sheets. After a few cycles, the

conductance-gate response of either single- or bi-layer graphene becomes sharper and smoother, and such change is reversible. We attribute this effect to releasing of pre-existing tension or wrinkles in the devices. On the other hand, after the strain cycles, the minimum conductance of single layer samples is only minimally altered; in contrast, that of bilayer samples consistently decreases, which could result from relative shearing or sliding between the two atomic layers. Our results have implications for strain engineering of graphene, and can also be extended to other type of 2D materials.

I will begin this chapter by describing the device design and fabrication process in Section 7.1. In Section 7.2, transport measurement and data analysis will be shown on both single layer graphene devices and bi-layer graphene deivces. Finally, in Section 7.3, I will discuss possible mechanisms underlying these observations and conclude our work.

7.1 Device Design and Fabrication

Graphene sheets were extracted from bulk graphite using standard mechanical exfoliation techniques on top of SiO_2/Si substrates or a layer of the LOR resist. The number of layers was initially identified via optical microscopy and subsequently confirmed with Raman spectroscopy after completion of transport measurements (Figure 7.1a).

To perform transport measurement and *in situ* stretching, we developed a new type of nano-electromechanical systems (NEMS) with two different fabrication methods. In Method A, devices were fabricated with multi-level lithography based on the resists consist of LOR layer on top of PMMA layer. The detailed fabrication process is described in our previous work[13]. (Figure 7.1b). Devices thus fabricated have relatively large areas, and both the electrodes and graphene are suspended above the substrates (Figure 7.1c). The central electrode was designed wider and shorter than the neighboring electrodes, so that it can sustain higher actuating voltages.

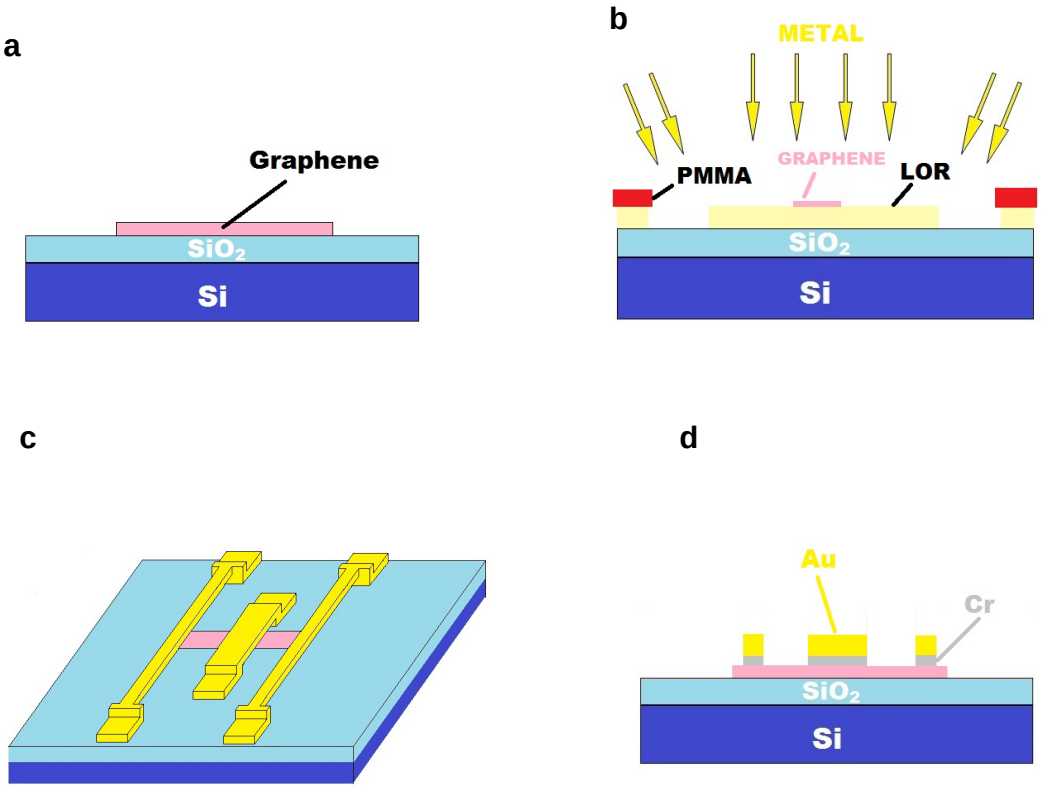

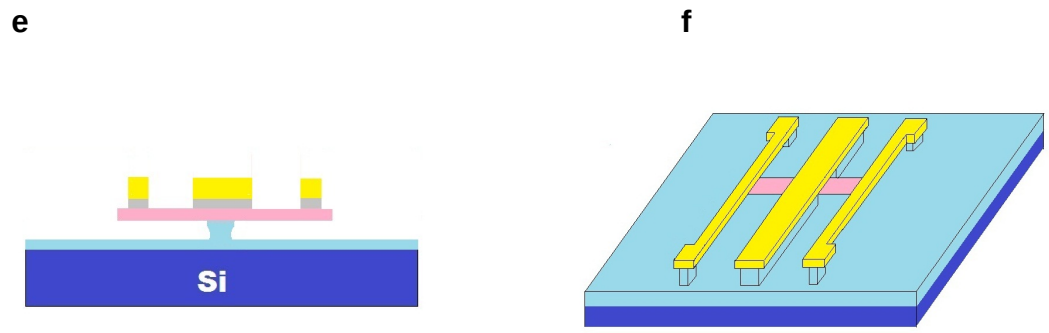

FIGURE 7.1. (a). Graphene sample exfoliation and identification. (b). Fabrication process using Method A and angled deposition. (c). Three dimensional schematic of a device fabricated with Method A. (d). Fabrication of a device using Method B, which is initially non-suspended. (e) BOE etching selectively removes SiO_2 underneath graphene samples and electrodes. (f). Three dimensional schematic of a device fabricated with Method B.

In Method B, which is used to fabricate the majority of the devices, three Cr/Au (10nm/150nm) electrodes were attached to graphene flakes using standard electron beam lithography (Figure 7.1d). Then the whole device was submerged into buffered oxidant etchant (BOE) solution for 90~120s.[14-16] For each device, the central electrode is designed to be 2-3 times wider (800nm~1000 nm wide, 25 ~40 μm long) than the two neighboring electrodes (300~400nm, 20 ~30 μm long). All electrodes are anchored by large contact pads at the ends. By controlling etching time, we can

control the extent of SiO_2 etched underneath the electrodes and graphene flake, so that narrower features and graphene flakes are suspended, whereas the wider features (central electrodes and anchors) remain supported by residual of SiO_2 underneath (Figure 7.1e). After etching, the device was transferred into water and isopropyl alcohol (IPA) in succession, in order to rinse and cover the sample with a liquid with lower surface tension. Finally, the device was taken out from hot IPA (to further decrease surface tension of IPA) and placed onto a hot plate at 70℃. The fabrication process is very robust: despite the fragility of suspended graphene devices, the yield is ~90%. Figure 7.1f illustrates the schematics of a typical device.

Figure 7.2a illustrates the general principle of applying *in situ* strain. A suspended electrode and the back gate (Si substrate) formed a capacitor. Initially both electrodes and the back gate are grounded, thus they remain parallel, as outlined by solid lines in Figure 7.2a. Upon applying the actuating voltage (bias voltage between electrodes and back gate), the electrostatic force induces deflection in the outer suspended or longer electrodes toward the substrate, whereas the central electrode (that is shorter, wider and/or partially supported by the substrate) remain suspended; thus the far ends of the attached graphene sheet move downward accordingly. From the geometry of our device, we can estimate the strain γ exerted on graphene

$$\gamma = \sqrt{1 + \frac{h^2}{L_0^{\,2}}} - 1 \qquad (1)$$

where *h* denotes the maximum vertical deflection of the suspended electrode under the electrostatic force, L_0 indicates the initial length of suspended graphene sample. We estimate that at maximum load, up to 5% strain can be induced in the graphene sheets.

Figure 7.2b-c show a device fabricated using method A at gate voltage V_g=0 and 30V, respectively. Initially all electrodes and the graphene sheet are well-suspended. When the gate voltage ramps, the narrower electrode on the left slowly deflects downward; at V_g=30 V, it buckles and collapses to the substrate. This collapse is irreversible even when V_g is reduced to 0. We note that when the measurement on a device is repeated on a device with the same geometry but without the graphene flake, the suspended electrode collapses at much smaller voltage V_g~7V. Since the electrostatic force is proportional to V_g^2, we estimate that at V_g=30V, ~95% of the electrostatic force is exerted on the graphene sheet. Figure 7.2d shows another device before and upon applying V_g~100V. Periodic ripples appears in the graphene sheet afterwards arises from the longitudinal strain induced[8].

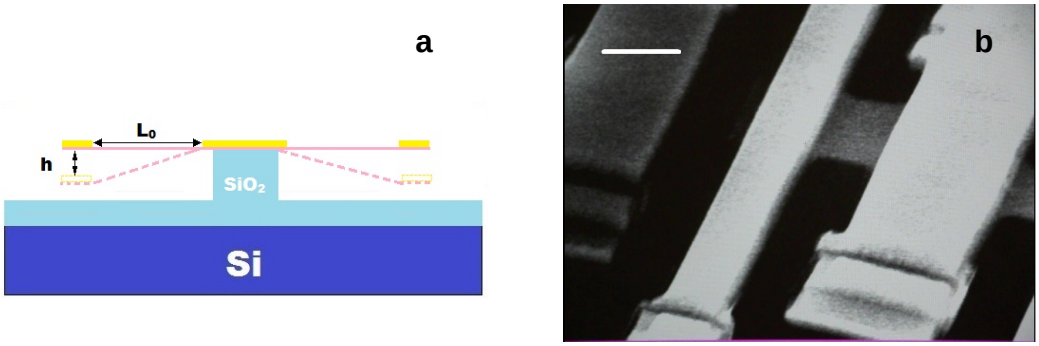

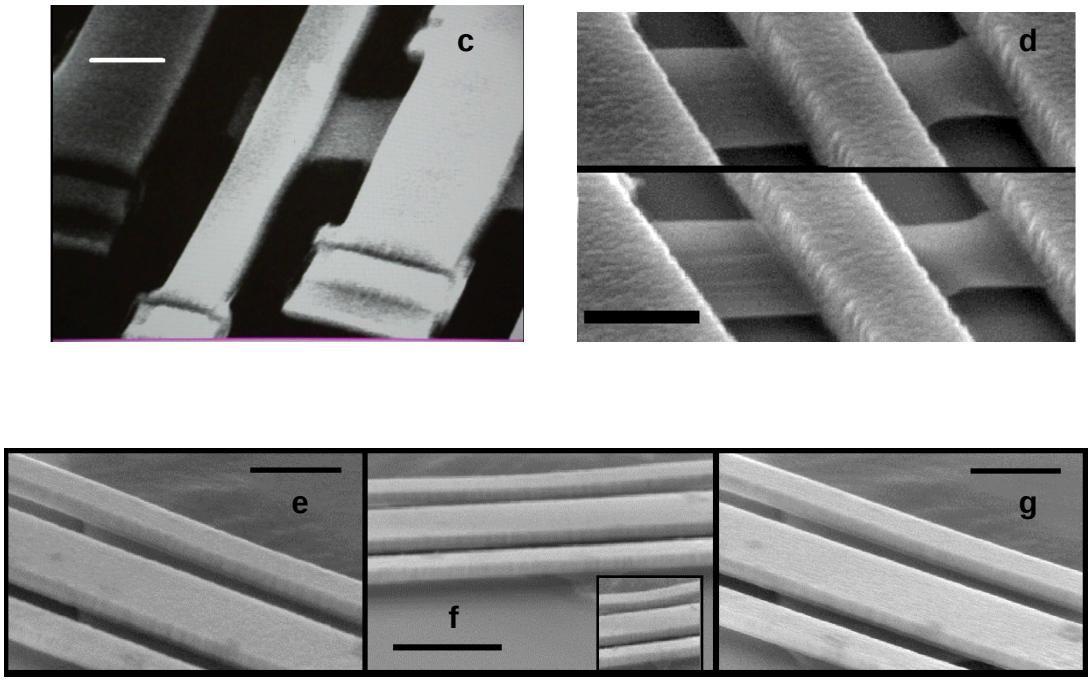

FIGURE 7.2. (a). Schematic of a device with and without applying the actuating voltage between electrodes and back gate. (b-c) SEM images of a device fabricated with Method A at V_g=0 and V_g=30V, respectively. Scale bars: 2μm. (d). SEM images of another graphene sample fabricated before (upper panel) and after stretched (lower panel). Scale bars: 2μm. (e,f,g) SEM images of a device made by Method B at V_g=0, V_g=50V, and when V_g is returned to 0. Scale bars: 1μm in (e) and (g), 2μm in (f). The inset in (f) shows a zoom-in image of the deflected region.

For devices fabricated with method B, the suspended electrodes can reversibly move between parallel and deflected positions. Figure 7.2e shows a device made by method B before stretching. Figure 7.2f displays SEM image of the same device is stretching a suspended sample under a V_g ~50V. A zooming in image shows one narrower electrode clearly deflected toward the substrate (inset in f). Figure 7.2g displays the same device when V_g is returned to 0V, and the suspended electrode returns to its original height. To avoid collapsing the samples, we typically limit the actuating voltage to less than 60V.

7.2 Transport Properties Under *in situ* Train

To perform transport measurements, the devices are cooled down to 4.2K in vacuum. Current annealing was applied to remove contaminants on the graphene sheet. The devices are first characterized by measuring its conductance G as a function of V_g; (Figure 7.3a, red curve) here V_g is limited to <±10V, so that strain is negligible. All devices show repeatable $G(V_g,)$ curves over such small V_g range.

After extracting data from its initial state, we start stretching the sample by gradually ramping up actuating voltage to -50V. Figure 7.3b shows the conductance changes as time elapsed, when the actuating voltage is maintained at 50V. The conductance fluctuates noticeably and decreased by more than 20 μS (~ 1%). We note that this effect cannot be explained by the changing capacitance between graphene and the gate – at the strained position, the device has stronger coupling to the gate,

thus should give rise to a *higher* conductance value. Thus the modulation in conductance must be induced by movement of the electrode itself, *e.g.* strain and/or changing the graphene-electrode interface.

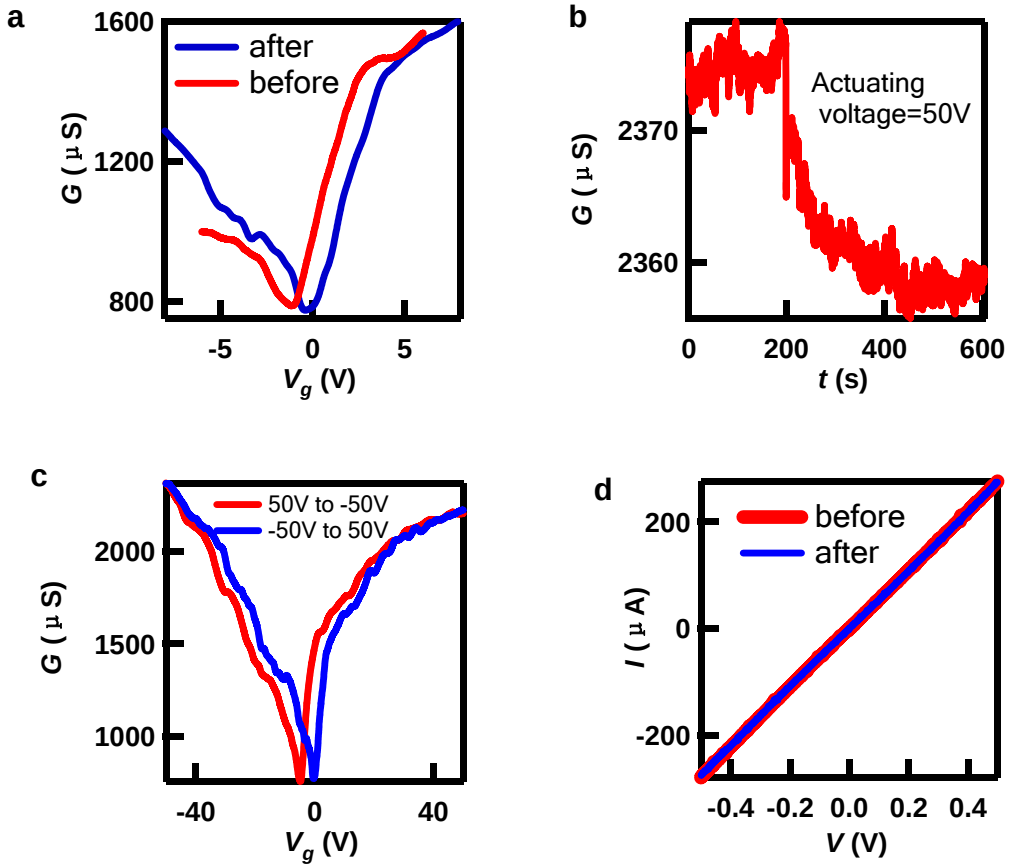

FIGURE 7.3. (a) Conductance as a function of back gate voltage, before (red curve) and after (blue curve) stretching process, from a single layer graphene device. (b).

Conductance *vs.* time when the actuating voltage is kept at 50V. (c). Conductance as a function of back gate after several stretching cycles. (d). *IV* curves of a typical single layer device before and after stretching process.

The tension in the sample is then released by lowering the actuating voltage back to 0V, and characterized again by measuring $G(V_g)$ for limited V_g range (Figure 7.3a, blue curve). For single layer graphene, minor changes such as slightly improved mobility are observed, but generally the minimum conductivity and the current-voltage *(I-V)* characteristics (Figure 7.3d) stay relatively constant. After several repeated sweeping cycles (between +/- 50V), the gate response became stable (Figure 7.3c) even at large gate voltage.

Compared with single layer samples, bilayer devices demonstrate even more interesting changes. Figure 7.4a shows the $G(V_g)$ curves before and after stretching from a typical bilayer devices. After releasing from external strain, the curve becomes steeper and smoother, and the mobility improves. Interestingly, the minimum conductance decreased considerably. This can also been seen in the *I-V* curves, which is more non-linear after stretching (Figure 7.4b). Typically, after stretching process, the conductance of bilayer devices decreases by 10%~20%. After several stretching cycles several times, the device's $G(V_g)$ becomes stable (Figure 7.4c) with the improved mobility and lower minimum conductance. The device shows no appreciable change in appearance after the stretching cycles (Figure 7.4d).

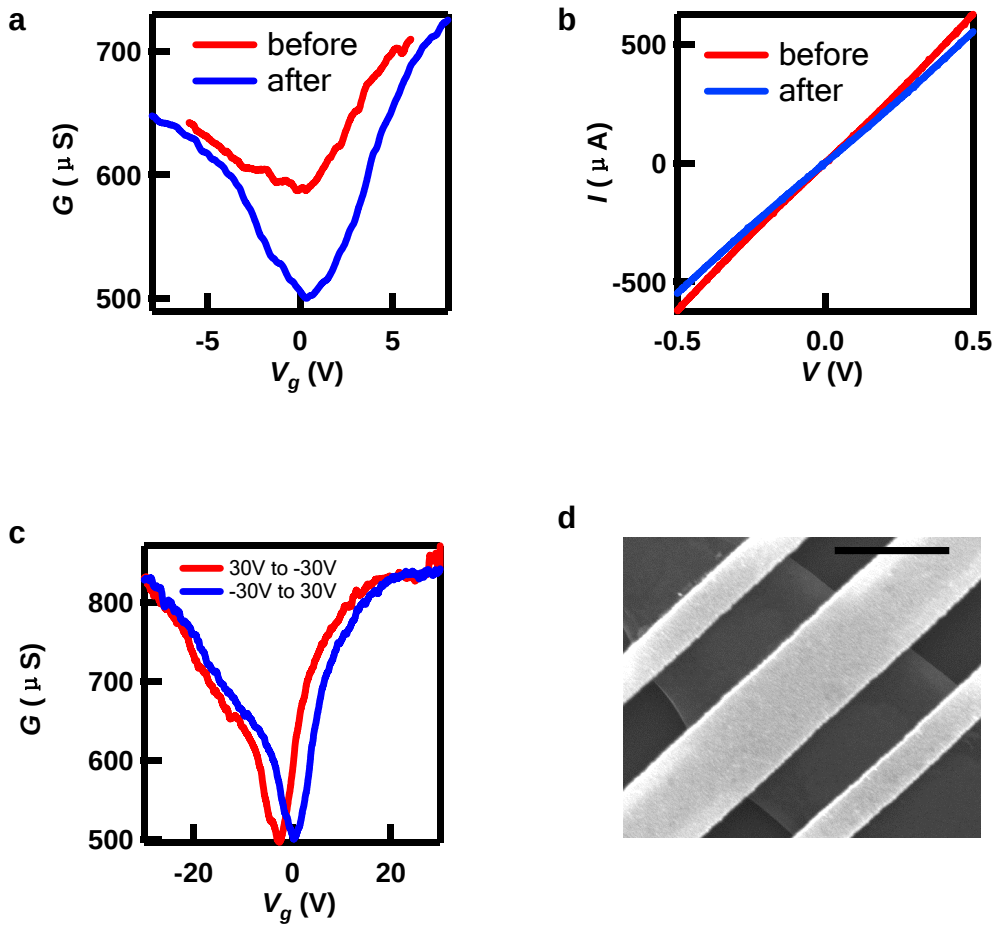

FIGURE 7.4. (a) Conductance as a function of back gate voltage, before (red curve) and after (blue curve) stretching process, from a bi-layer graphene device. (b). *IV* curves from one typical bi-layer device before and after the stretching process. (c). Conductance as a function of back gate after several cycles. (d) SEM image of one bi-layer graphene device after stretching. Scale bar: 1μm.

7.3 Possible Mechanisms

These intriguing observations suggest the rich interplay between strain and transport offered by suspended devices. The improvement in device mobility likely arises from releasing the strain or ripples that are built-in during the fabrication process. The different behaviors between single layer and bilayer devices are particularly intriguing, *e.g.* the significant decrease in minimum conductance is unique to bilayer devices. A possible explanation is the improved contact at the electrode-graphene interface; however, one expects that this scenario should occur in single-layer devices as well. We also exclude strain-induced cracks, which should occur at much higher strain[17] and also lead to lower mobility. Our present proposal is that the decrease in minimum conductance may be caused by relative shift and/or shear between two layers induced by the stretching cycles.[18-20] This hypothesis can be verified by low temperature transport measurements, as the modified band structure is expected to lead to reduced density of states and different Landau level spectrum than that of an AB-stacked bilayer graphene.

In conclusion, we developed two types of NEMS-like devices to stretch suspended single crystal graphene samples and perform *in situ* measurements. The stretching process can be observed via SEM imaging. Transport property investigation shows that after stretching process, the gate response of conductance

from graphene samples improved, and dramatic decrease in minimum conductance is observed in bi-layer graphene samples. The experimental system and method introduced in this work provides a new approach in strain engineering researches.

References

1 Novoselov, K. S.; Geim, A. K.; Morozov, S. V.; Jiang, D.; Zhang, Y.; Dubonos, S. V.; Grigorieva, I. V.; Firsov, A. A. *Science* **2004**, *306*, 666.

2 Berger, C.; Song, Z.; Li, X.; Wu, X.; Brown, N.; Naud, C.; Mayou, D.; Li, T.; Hass, J.; Marchenkov, A. N.; Conrad, E. H.; First, P. N.; de Heer, W. A. *Science* **2006**, *312*, 1191.

3 Geim, A. K.; Novoselov, K. S. *Nat Mater* **2007**, *6*, 183.

4 Novoselov, K. S.; Geim, A. K.; Morozov, S. V.; Jiang, D.; Katsnelson, M. I.; Grigorieva, I. V.; Dubonos, S. V.; Firsov, A. A. *Nature* **2005**, *438*, 197.

5 Zhang, Y.; Tan, Y. W.; Stormer, H. L.; Kim, P. *Nature* **2005**, *438*, 201.

6 Fuhrer, M. S. *Nat Mater* **2010**, *9*, 611.

7 Pereira, V. M.; Castro Neto, A. H. *Phys Rev Lett* **2009**, *103*, 046801.

8 Bao, W.; Miao, F.; Chen, Z.; Zhang, H.; Jang, W.; Dames, C.; Lau, C. N. *Nat Nanotechnol* **2009**, *4*, 562.

9 Gui, G. P.; Kadayaprath, G.; Tan, S. M.; Faliakou, E. C.; Choy, C.; Ward, A.; A'Hern, R. *Plast Reconstr Surg* **2008**, *121*, 17.

10 Guinea, F.; Katsnelson, M. I.; Geim, A. K. *Nat Phys* **2010**, *6*, 30.

11 Mohiuddin, T. M. G.; Lombardo, A.; Nair, R. R.; Bonetti, A.; Savini, G.; Jalil, R.; Bonini, N.; Basko, D. M.; Galiotis, C.; Marzari, N.; Novoselov, K. S.; Geim, A. K.; Ferrari, A. C. *Physical Review B* **2009**, *79*, 205433.

12 Zabel, J.; Nair, R. R.; Ott, A.; Georgiou, T.; Geim, A. K.; Novoselov, K. S.; Casiraghi, C. *Nano Lett* **2012**, *12*, 617.

13 Velasco, J., Jr.; Zhao, Z.; Zhang, H.; Wang, F.; Wang, Z.; Kratz, P.; Jing, L.; Bao, W.; Shi, J.; Lau, C. N. *Nanotechnology* **2011**, *22*, 285305.

14 Bolotin, K. I.; Sikes, K. J.; Jiang, Z.; Klima, M.; Fudenberg, G.; Hone, J.; Kim, P.; Stormer, H. L. *Solid State Commun.* **2008**, *146*, 351.

15 Du, X.; Skachko, I.; Barker, A.; Andrei, E. Y. *Nat. Nano.* **2008**, *3*, 491.

16 Zhang, H.; Bao, W.; Zhao, Z.; Huang, J.-W.; Standley, B.; Liu, G.; Wang, F.; Kratz, P.; Jing, L.; Bockrath, M.; Lau, C. N. *Nano Letters* **2012**, *12*, 1772.

17 Lee, C.; Wei, X.; Kysar, J. W.; Hone, J. *Science* **2008**, *321*, 385.

18 Cocco, G.; Cadelano, E.; Colombo, L. *Physical Review B* **2010**, *81*, 241412.

19 Huang, M.; Pascal, T. A.; Kim, H.; Goddard, W. A.; Greer, J. R. *Nano Letters* **2011**, *11*, 1241.

20 Gui, G.; Li, J.; Zhong, J. *Physical Review B* **2008**, *78*, 075435.

Chapter 8

Conclusion and Outlook

In summary, my doctorial research work focuses on modified graphene devices that may be applied towards electronic devices. It consists of three separate yet related topics: chemically functionalized graphene, suspended graphene -based switches and transport properties of suspended graphene under *in situ* strain.

Chemical functionalization by grafting aryl groups onto carbon sites in graphene flakes can change the hybridization of C-C bonds, which will in turn modify the band structure of pristine graphene to open a band gap. A different approach based upon organometallic chemistry provides enhanced on/off ratios, while retaining the high mobility of pristine graphene samples. Thus, functionalized graphene is a promising candidate material for next generation semiconductor devices or serve as chemical/bio- sensors.

Suspended graphene-based switch serves as a nice platform that reveals the mechanism of the repeatable switching behavior from electrically breakdown

carbon system. Suspended structure completely isolates the all-carbon-system; combined with temperature dependent studies on switching behaviors, the mechanism is confirmed to be the motion of atomic scale carbon chains and rearrangement of carbon bonds. To breakdown the delicate suspended graphene membrane, we also developed a pulsing-breakdown method, which can be adopted in other suspended structures. In the application front, graphene based switches can work as long term information storage devices.

Based on a new type of nano-electromechanical system (NEMS) devices proposed and developed by us, we studied suspended graphene samples under in situ strains. Strains were confirmed by *in situ* SEM imaging system. The changes on mobility and gate response were observed in single and bilayer devices that are subjected to repeated strain. In particular, strain can significantly lower the conductance of bilayer graphene at the charge neutrality point. This type of NEMS devices can be extended to other materials to study their transport or optical properties under *in situ* strain.

These discoveries demonstrate interesting sciences amid carbon systems and suggest a number of directions for future work. For instance, modified graphene devices with *both* high mobility and a true band gap, is still not yet synthesized. Observing and manipulating the motion carbon chains in atomic scale with help of high resolution tools such as TEM will provide not only the final confirmation for

our model outlined in Ch 6, but also a platform for investigating electronic behavior in 1D atomic chains. In the long term (and in the hope of the writer), developing and commercializing all-carbon electronic devices, e.g. graphene-based CPU, all-carbon storage devices, could give rise to another revolution in future IT industry.

Appendix I

Source Code and introduction of Graphene Layer Viewer

Graphene layer viewer is a tool designed to help researchers to determine the number layers of graphene samples. Since it was developed in java, it is compatible with Windows/Mac/Linux operating systems. The user simply needs to select the substrate area and sample area from an optical image, and the software displays the number of layers of the selected sample based on relative intensities of the RGB channels of the two areas. The detailed manual can be downloaded from the following link:

https://sites.google.com/site/graphenelayer/faq

```
import java.awt.*;
import java.awt.event.*;
import javax.swing.*;
import java.io.*;
import javax.imageio.*;
import java.awt.image.*;
import javax.swing.event.HyperlinkEvent;
```

```
import javax.swing.event.HyperlinkListener;

public class GLayer2 extends JFrame implements ActionListener{
	JButton substrate,sample;
	JPanel p1,p2,p3;
	JEditorPane editorPane1;
	JScrollPane scrollPane;
	BufferedImage get1,get2;
	int s1=0,s2=0;
	float sumRC1=0,sumBC1=0,sumGC1=0,aveRC1=0,aveBC1=0,aveGC1=0;
	float sumRC2=0,sumBC2=0,sumGC2=0,aveRC2=0,aveBC2=0,aveGC2=0;

	public GLayer2() {
		super("V1.0    BY HANG ZHANG & JHAO-WUN HUANG");
		initWindow();
	}
	public void initWindow(){

		substrate=new JButton("SUBSTRATE");
		sample=new JButton("      SAMPLE      ");

		substrate.addActionListener(this);
		sample.addActionListener(this);
		JPanel buttonJP =new JPanel();

		p1=new JPanel(new BorderLayout());
		p2=new JPanel();
		p3=new JPanel();
		/*editorPane1 = new JEditorPane();
		editorPane1.setEditable(false);
		editorPane1.setContentType("text/html");
		editorPane1.setText("<html><body><a
href=http://pubs.acs.org/doi/abs/10.1021/nl200803q>Aryl Functionalization as a
Route to Band Gap Engineering in Single Layer Graphene
Devices</a><p></p><a
href=http://pubs.acs.org/doi/abs/10.1021/nl203160x>Visualizing Electrical
Breakdown and ON/OFF States in Electrically Switchable Suspended Graphene
Break Junctions</a></body></html>");

		editorPane1.addHyperlinkListener(new HyperlinkListener() {
```

```
                public void hyperlinkUpdate(HyperlinkEvent e) {
                  if (e.getEventType() ==
HyperlinkEvent.EventType.ACTIVATED) {
                    try {
                      String command = "explorer.exe "
                          + e.getURL().toString();
                      Runtime.getRuntime().exec(command);
                    } catch (Exception ex) {
                      ex.printStackTrace();
                      System.err.println("connection error");
                    }
                  }

                }
            });

            scrollPane = new JScrollPane(editorPane1);*/

            JLabel title=new JLabel("GLAYER V2.0",JLabel.CENTER);
            /*JLabel group=new JLabel("PLEASE CITE OUR PAPERS, IF YOU
FEEL THIS TOOL IS HELPFUL :)",JLabel.CENTER);*/

            title.setFont(new Font("ARIAL",Font.BOLD,24));
            /*group.setFont(new Font("ARIAL",Font.BOLD,12));*/
            title.setForeground(Color.RED);
            /*group.setForeground(Color.BLUE);*/

            p1.add(title,BorderLayout.NORTH);
           /* p1.add(group,BorderLayout.CENTER);*/

            p2.add(new JLabel(new
ImageIcon(getClass().getResource("init.jpg"))));
            p3.add(new JLabel(new
ImageIcon(getClass().getResource("init.jpg"))));
            buttonJP.add(substrate);
            buttonJP.add(sample);

            this.add(p1,BorderLayout.NORTH);
            this.add(p2,BorderLayout.WEST);
```

```
        /*this.add(scrollPane,BorderLayout.CENTER);*/
        this.add(p3,BorderLayout.EAST);
        this.add(buttonJP,BorderLayout.SOUTH);
        this.setSize(240,220);
        this.setLocationRelativeTo(null);
        this.setVisible(true);
        this.setAlwaysOnTop(true);
        this.setDefaultCloseOperation(JFrame.EXIT_ON_CLOSE);
        SwingUtilities.updateComponentTreeUI(this);
    }
    public void updates(){
        this.setVisible(true);
        if(s1!=0){
            ImageIcon ii1=new ImageIcon(get1);
            int width =get1.getWidth();
            int height =get1.getHeight();
            sumRC1=0;
            sumBC1=0;
            sumGC1=0;
            ColorModel cm = ColorModel.getRGBdefault();
            for (int i=0;i<width;i++){
                for (int j=0;j<height;j++){
                    sumRC1=sumRC1+(float)(cm.getRed(get1.getRGB(i, j)));
                    sumBC1=sumBC1+(float)(cm.getBlue(get1.getRGB(i, j)));
                    sumGC1=sumGC1+(float)(cm.getGreen(get1.getRGB(i,
j)));
                }
            }
            aveRC1=sumRC1/width/height;
            aveBC1=sumBC1/width/height;
            aveGC1=sumGC1/width/height;

            ii1.setImage(ii1.getImage().getScaledInstance(100, 100,
                    Image.SCALE_DEFAULT));
            JLabel im1=new JLabel(ii1);

            p2.removeAll();
            p2.add(new JScrollPane(im1),BorderLayout.NORTH);

              SwingUtilities.updateComponentTreeUI(this);
```

```
            }
            if(s2!=0){
                ImageIcon ii2=new ImageIcon(get2);
                int width =get2.getWidth();
                int height=get2.getHeight();
                sumRC2=0;
                sumBC2=0;
                sumGC2=0;
                ColorModel cm = ColorModel.getRGBdefault();
                for (int i=0;i<width;i++){
                    for (int j=0;j<height;j++){
                        sumRC2=sumRC2+(float)(cm.getRed(get2.getRGB(i, j)));
                        sumBC2=sumBC2+(float)(cm.getBlue(get2.getRGB(i, j)));
                        sumGC2=sumGC2+(float)(cm.getGreen(get2.getRGB(i,
j)));
                    }
                }
                aveRC2=sumRC2/width/height;
                aveBC2=sumBC2/width/height;
                aveGC2=sumGC2/width/height;

                ii2.setImage(ii2.getImage().getScaledInstance(100, 100,
                        Image.SCALE_DEFAULT));
                JLabel im2=new JLabel(ii2);

                p3.removeAll();
                p3.add(new JScrollPane(im2),BorderLayout.NORTH);

                p1.removeAll();

                  JLabel ratio;
                  String info="";
                  float r=
Math.abs((aveRC1-aveRC2)/aveRC2)+Math.abs((aveGC1-aveGC2)/aveGC2)+M
ath.abs((aveBC1-aveBC2)/aveBC2);

                  if(r < 0.02){
                     info="NOT A GRAPHENE SAMPLE";
                  }
```

```
                if(r >= 0.02 && r < 0.117632){
                   info="LAYER = 1";
                }
                if(r >= 0.117632 && r < 0.204503){
                   info="LAYER = 2";
                }
                if(r >= 0.204503 && r < 0.291434){
                   info="LAYER = 3";
                }
                if(r >= 0.291434){
                   info="MULTI-LAYER";
                }
                JLabel title=new JLabel(info,JLabel.CENTER);
               /* ratio=new JLabel("THE RATIO OF THE COLOR CHANNEL IS
"+r,JLabel.CENTER);*/

                title.setFont(new Font("ARIAL",Font.BOLD,32));
                /*ratio.setFont(new Font("ARIAL",Font.BOLD,12));*/
                title.setForeground(Color.BLUE);
                /*ratio.setForeground(Color.BLUE);*/

                p1.add(title,BorderLayout.NORTH);
                /*p1.add(ratio,BorderLayout.CENTER);*/

                SwingUtilities.updateComponentTreeUI(this);
            }
        }


        private void snapshot(){
            try{
                this.setVisible(false);
                Thread.sleep(500);
                Robot robot =new Robot();
                Toolkit tk=Toolkit.getDefaultToolkit();
                Dimension di=tk.getScreenSize();
                Rectangle rec=new Rectangle(0,0,di.width,di.height);
                BufferedImage bi=robot.createScreenCapture(rec);
                JFrame jf=new JFrame();
                Temp temp=new Temp(jf,bi,di.width,di.height);
```

```
                jf.getContentPane().add(temp,BorderLayout.CENTER);
                jf.setUndecorated(true);
                jf.setSize(di);
                jf.setVisible(true);
                jf.setAlwaysOnTop(true);
            } catch(Exception e){
                e.printStackTrace();
            }
        }

        public void actionPerformed(ActionEvent ae){
            if(ae.getSource()==substrate){
                s1=1;
                s2=0;
                snapshot();

            }else if(ae.getSource()==sample){
                s1=0;
                  s2=1;
                  snapshot();

            }
        }

        class PicturePanel extends JPanel {
            public void paint(Graphics g, Image img) {
               g.drawImage(img, 0, 0, this);
            }
          }
        private class Temp extends JPanel implements
MouseListener,MouseMotionListener{
            private BufferedImage bi;
            private int width,height;
            private int startX,startY,endX,endY,tempX,tempY;
            private JFrame jf;
            private Rectangle select=new Rectangle(0,0,0,0);
            private Cursor cs=new Cursor(Cursor.CROSSHAIR_CURSOR);
            private States current=States.DEFAULT;
            private Rectangle[] rec;
```

```
        public static final int START_X=1;
        public static final int START_Y=2;
        public static final int END_X=3;
        public static final int END_Y=4;
        private int currentX,currentY;
        private Point p=new Point();
        private boolean showTip=true;
        public Temp(JFrame jf,BufferedImage bi,int width,int height){
            this.jf=jf;
            this.bi=bi;
            this.width=width;
            this.height=height;
            this.addMouseListener(this);
            this.addMouseMotionListener(this);
            initRecs();
        }
        private void initRecs(){
            rec=new Rectangle[8];
            for(int i=0;i<rec.length;i++){
                rec[i]=new Rectangle();
            }
        }
        public void paintComponent(Graphics g){
            g.drawImage(bi,0,0,width,height,this);
            g.setColor(Color.RED);
            g.drawLine(startX,startY,endX,startY);
            g.drawLine(startX,endY,endX,endY);
            g.drawLine(startX,startY,startX,endY);
            g.drawLine(endX,startY,endX,endY);
            int x=startX<endX?startX:endX;
            int y=startY<endY?startY:endY;
            select=new
Rectangle(x,y,Math.abs(endX-startX),Math.abs(endY-startY));
            int x1=(startX+endX)/2;
            int y1=(startY+endY)/2;
            g.fillRect(x1-2,startY-2,5,5);
            g.fillRect(x1-2,endY-2,5,5);
            g.fillRect(startX-2,y1-2,5,5);
            g.fillRect(endX-2,y1-2,5,5);
            g.fillRect(startX-2,startY-2,5,5);
```

```
                g.fillRect(startX-2,endY-2,5,5);
                g.fillRect(endX-2,startY-2,5,5);
                g.fillRect(endX-2,endY-2,5,5);
                rec[0]=new Rectangle(x-5,y-5,10,10);
                rec[1]=new Rectangle(x1-5,y-5,10,10);
                rec[2]=new Rectangle((startX>endX?startX:endX)-5,y-5,10,10);
                rec[3]=new Rectangle((startX>endX?startX:endX)-5,y1-5,10,10);
                rec[4]=new
Rectangle((startX>endX?startX:endX)-5,(startY>endY?startY:endY)-5,10,10);
                rec[5]=new Rectangle(x1-5,(startY>endY?startY:endY)-5,10,10);
                rec[6]=new Rectangle(x-5,(startY>endY?startY:endY)-5,10,10);
                rec[7]=new Rectangle(x-5,y1-5,10,10);
                if(showTip){
                    g.setColor(Color.CYAN);
                    g.fillRect(p.x,p.y,170,20);
                    g.setColor(Color.RED);
                    g.drawRect(p.x,p.y,170,20);
                    g.setColor(Color.BLACK);
                    g.drawString("PLEASE SELECT THE
REGION",p.x,p.y+15);
                }
            }

            private void initSelect(States state){
                switch(state){
                    case DEFAULT:
                        currentX=0;
                        currentY=0;
                        break;
                    case EAST:
                        currentX=(endX>startX?END_X:START_X);
                        currentY=0;
                        break;
                    case WEST:
                        currentX=(endX>startX?START_X:END_X);
                        currentY=0;
                        break;
                    case NORTH:
                        currentX=0;
                        currentY=(startY>endY?END_Y:START_Y);
```

```
                break;
            case SOUTH:
                currentX=0;
                currentY=(startY>endY?START_Y:END_Y);
                break;
            case NORTH_EAST:
                currentY=(startY>endY?END_Y:START_Y);
                currentX=(endX>startX?END_X:START_X);
                break;
            case NORTH_WEST:
                currentY=(startY>endY?END_Y:START_Y);
                currentX=(endX>startX?START_X:END_X);
                break;
            case SOUTH_EAST:
                currentY=(startY>endY?START_Y:END_Y);
                currentX=(endX>startX?END_X:START_X);
                break;
            case SOUTH_WEST:
                currentY=(startY>endY?START_Y:END_Y);
                currentX=(endX>startX?START_X:END_X);
                break;
            default:
                currentX=0;
                currentY=0;
                break;
        }
    }
    public void mouseMoved(MouseEvent me){
        doMouseMoved(me);
        initSelect(current);
        if(showTip){
            p=me.getPoint();
            repaint();
        }
    }

    private void doMouseMoved(MouseEvent me){
        if(select.contains(me.getPoint())){
            this.setCursor(new Cursor(Cursor.MOVE_CURSOR));
            current=States.MOVE;
```

```
        } else{
            States[] st=States.values();
            for(int i=0;i<rec.length;i++){
                if(rec[i].contains(me.getPoint())){
                    current=st[i];
                    this.setCursor(st[i].getCursor());
                    return;
                }
            }
            this.setCursor(cs);
            current=States.DEFAULT;
        }
    }
    public void mouseExited(MouseEvent me){

    }
    public void mouseEntered(MouseEvent me){

    }
    public void mouseDragged(MouseEvent me){
        int x=me.getX();
        int y=me.getY();
        if(current==States.MOVE){
            startX+=(x-tempX);
            startY+=(y-tempY);
            endX+=(x-tempX);
            endY+=(y-tempY);
            tempX=x;
            tempY=y;
        }else if(current==States.EAST||current==States.WEST){
            if(currentX==START_X){
                startX+=(x-tempX);
                tempX=x;
            }else{
                endX+=(x-tempX);
                tempX=x;
            }
        }else if(current==States.NORTH||current==States.SOUTH){
            if(currentY==START_Y){
                startY+=(y-tempY);
```

```
                    tempY=y;
                }else{
                    endY+=(y-tempY);
                    tempY=y;
                }
            }else
if(current==States.NORTH_EAST||current==States.NORTH_EAST||

current==States.SOUTH_EAST||current==States.SOUTH_WEST){
                if(currentY==START_Y){
                    startY+=(y-tempY);
                    tempY=y;
                }else{
                    endY+=(y-tempY);
                    tempY=y;
                }
                if(currentX==START_X){
                    startX+=(x-tempX);
                    tempX=x;
                }else{
                    endX+=(x-tempX);
                    tempX=x;
                }

            }else{
                startX=tempX;
                startY=tempY;
                endX=me.getX();
                endY=me.getY();
            }
            this.repaint();
        }
        public void mousePressed(MouseEvent me){
            showTip=false;
            tempX=me.getX();
            tempY=me.getY();
        }
        public void mouseReleased(MouseEvent me){
            if(me.isPopupTrigger()){
                if(current==States.MOVE){
```

```
                    showTip=true;
                    p=me.getPoint();
                    startX=0;
                    startY=0;
                    endX=0;
                    endY=0;
                    repaint();
                } else{
                    jf.dispose();
                    updates();
                }

            }
        }
        public void mouseClicked(MouseEvent me){
            if(me.getClickCount()==2){

                Point p=me.getPoint();
                if(select.contains(p)){

if(select.x+select.width<this.getWidth()&&select.y+select.height<this.getHeight()
){
                        if (s1==1 && s2==0){

get1=bi.getSubimage(select.x,select.y,select.width,select.height);}
                        if (s1==0 && s2==1){

get2=bi.getSubimage(select.x,select.y,select.width,select.height);}
                            jf.dispose();

                            updates();
                        }else{
                            int wid=select.width,het=select.height;
                            if(select.x+select.width>=this.getWidth()){
                                wid=this.getWidth()-select.x;
                            }
                            if(select.y+select.height>=this.getHeight()){
                                het=this.getHeight()-select.y;
                            }
                            if (s1==1 && s2==0){
```

```
                                get1=bi.getSubimage(select.x,select.y,wid,het);}
                                if (s1==0 && s2==1){
                                get1=bi.getSubimage(select.x,select.y,wid,het);}
                                jf.dispose();

                                updates();
                            }

                        }
                    }
                }
        }

        public static void main(String args[]){
            GLayer2 gl =new GLayer2();
        }
}

enum States{
        NORTH_WEST(new Cursor(Cursor.NW_RESIZE_CURSOR)),
        NORTH(new Cursor(Cursor.N_RESIZE_CURSOR)),
        NORTH_EAST(new Cursor(Cursor.NE_RESIZE_CURSOR)),
        EAST(new Cursor(Cursor.E_RESIZE_CURSOR)),
        SOUTH_EAST(new Cursor(Cursor.SE_RESIZE_CURSOR)),
        SOUTH(new Cursor(Cursor.S_RESIZE_CURSOR)),
        SOUTH_WEST(new Cursor(Cursor.SW_RESIZE_CURSOR)),
        WEST(new Cursor(Cursor.W_RESIZE_CURSOR)),
        MOVE(new Cursor(Cursor.MOVE_CURSOR)),
        DEFAULT(new Cursor(Cursor.DEFAULT_CURSOR));
        private Cursor cs;
        States(Cursor cs){
                this.cs=cs;
        }
        public Cursor getCursor(){
                return cs;
        }
}
```